CHAPTER 3

RESULTS AND DISCUSSION

3.1 Cyclic microwave-assisted synthesis of Cu_3BiS_3 dendrites using L-cysteine as a sulfur source and complexing agent

To investigate structure information of the samples obtained in present research, X-ray powder diffraction (XRD) was carried out. Figure 3.1 is the representative XRD pattern of products synthesized at different microwave power using 40 time cycles. At 300 W, comparing the XRD pattern to the JCPDS file (No. 43-1479 and 02-1272) [81], there was very good correlation between the XRD pattern of the sample and the standard, in 2θ position as well as in relative intensities. As a result, this product was proved to be orthorhombic Cu_3BiS_3 mixed with Cu_2S impurity. The pattern was composed of rather weak peaks, specifying that the degree of crystallinity was quite low in this product. Diffraction peaks were indexed as shown in Figure 3.1. The strongest intensity peak is at 2θ = 31.31 degrees and diffracts from (131) plane of the powder. When the higher microwave powers were employed, the XRD patterns became sharper. At 700 W, the pattern was composed of the sharpest peaks and the degree of crystallinity was the highest.

Microwave power had a significant effect on the crystallinity of the Cu_3BiS_3 powder obtained in the ethylene glycol solution prepared by adding CuCl, $BiCl_3$ and L-cysteine to the solvent. By increasing microwave power from 300 W until microwaving at powers of 600 and 700 W, the impurities were lessened with the forming of pure single-phase orthorhombic Cu_3BiS_3. Differences in the intensity of

the XRD peaks were observed to correlate with microwave power and the sharp diffraction peaks indicate good crystallinity of the powders.

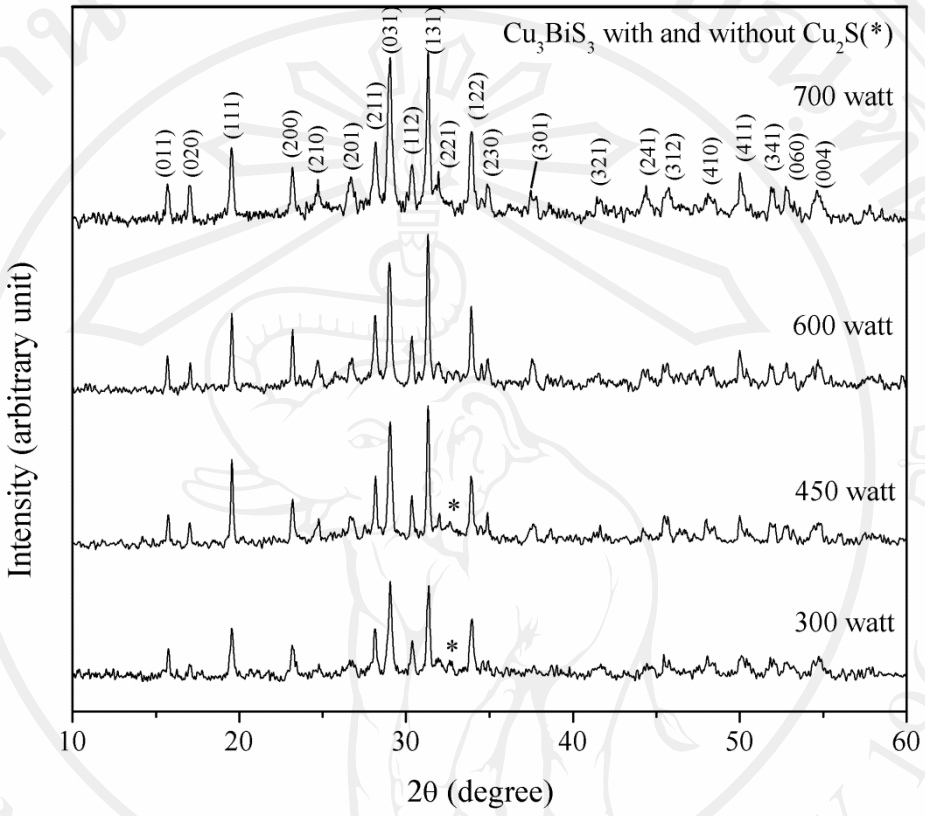

Figure 3.1 XRD spectra of the products prepared using different microwave power and 40 cycles of radiation.

The spaces between adjacent planes (d) and lattice parameter (a, b, c) of different diffraction peak of the product synthesized at microwave power 700 W, 40 cycles were calculated using Bragg's law and the plane-spacing equation for orthorhombic structure [82].

$$\frac{1}{d^2} = \frac{h^2}{a^2} + \frac{k^2}{b^2} + \frac{i^2}{c^2}$$ for orthorhombic phase crystal

As a result (Table 3.1), these interplanar spacing of different planes are in good accordance with those of the JCPDS standard [81].

Table 3.1 Calculated lattice parameter of Cu_3BiS_3 from the experiment (synthesized at microwave 700 W, 40 cycles), comparing with the JCPDS file (Reference code: 43-1479)

Plane	2θ		Interplanar spacing (d), Å		Lattice parameter, Å	
	Exp.	JCPDS file	Exp.	JCPDS file	Exp.	JCPDS file
020	17.068	17.061	5.1908	5.1930	b=10.3816	b = 10.3880
200	23.172	23.095	3.8354	3.8480	a=7.6708	a = 7.6960
111	19.510	19.502	4.5463	4.5480	c=6.7246	c = 6.7119

Exp. = experiment

Table 3.2 The 2θ diffraction angles and intensities of the JCPDS no. 43-1479 and the data of Cu_3BiS_3 (at microwave 700 W, 40 cycles) obtained from the experiment

Plane	JCPDS		Experiment	
	2θ (deg.)	Intensity (%)	2θ (deg.)	Intensity (%)
011	15.703	20	15.692	24.77
020	17.061	21	17.068	24.71
111	19.502	50	19.510	46.05
200	23.095	38	23.172	35.14
210	24.641	13	24.708	28.63
201	26.676	13	26.686	28.63

Table 3.2 (Continued) The 2θ diffraction angles and intensities of the JCPDS no. 43-1479 and the data of Cu_3BiS_3 (at microwave 700 W, 40 cycles) obtained from the experiment

Plane	JCPDS		Experiment	
	2θ (deg.)	**Intensity (%)**	**2θ (deg.)**	**Intensity (%)**
211	28.055	42	28.176	48.28
031	28.995	79	29.050	93.79
112	30.273	24	30.338	35.98
131	31.272	100	31.310	100.00
221	31.843	20	31.492	33.87
122	33.837	46	33.390	52.01
230	34.813	20	34.848	24.95
301	37.505	15	37.466	22.90
321	41.462	10	41.442	19.28
241	44.153	11	44.382	25.49
312	45.313	16	45.746	24.29
410	47.905	14	47.928	19.71
411	50.049	16	50.014	32.18
341	51.901	16	51.882	25.37
060	52.834	10	52.736	24.41
004	54.670	12	54.630	23.44

The FE-SEM images of Cu_3BiS_3 products obtained through a cyclic microwave radiation route, for 300 W – 700 W 40 cycles, are shown in Figure 3.2-3.5. The microwave power made a great effect on the morphologies of Cu_3BiS_3 powder. FE-SEM image of the as-prepared product synthesized at 300 W is shown in Figure 3.2, which revealed that the micro-sized product consisted of the agglomerate of nanoparticles with different orientations. Figure 3.3 displays the FE-SEM image of the sample prepared under 450 W, it can be clearly seen that the sample had a multi-armed dendrite-like structures. By increasing the microwave powers from 300 W to 450 and 600 W, (Figure 3.2-3.4), the products were gradually transformed into dendrites. At these stages, the products were mixtures of nanoparticles and dendrites. At 700 W (Figure 3.5), the whole product consisted of expanded dendrites in different orientations. This phenomenon proved that microwave radiation at higher powers has a strong influence on the atoms to form a crystal lattice, and that orthorhombic Cu_3BiS_3 unit cells were able to arrange themselves to fit with both nanoparticles and dendrites. According to that result, by control of microwave power offers a flexible method to obtain Cu_3BiS_3 nanostructures with different shapes (agglomerate nanoparticles or dendrites) suitable for different applications.

TEM and SAED images of the products obtained with different microwave power at the cyclic microwave radiation 40 cycles are shown. It should be noted that morphology appear on SEM images were in three dimensions, but those on TEM images were in two dimensions. The product obtained at 300 W of microwave power consisted of irregular Cu_3BiS_3 particle with obvious aggregation (Figure 3.6 right).

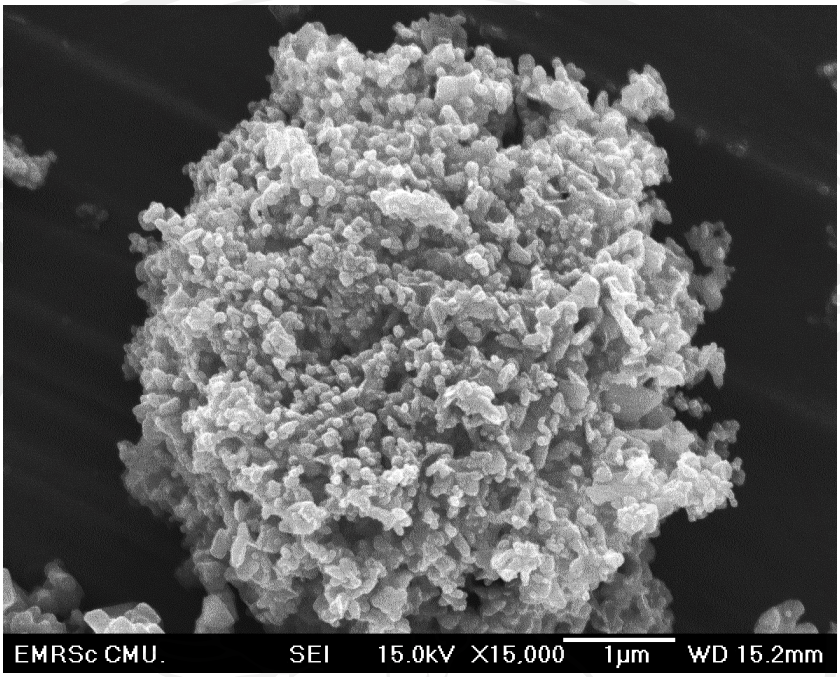

Figure 3.2 SEM image of Cu_3BiS_3 synthesized under condition of microwave power 300 W, 40 cycles.

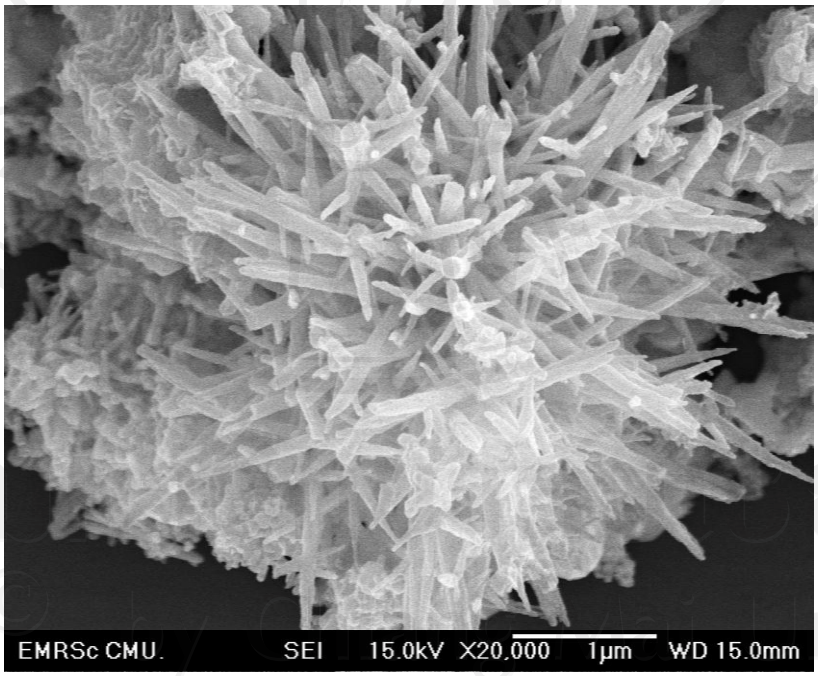

Figure 3.3 SEM image of Cu_3BiS_3 synthesized under condition of microwave power 450 W, 40 cycles.

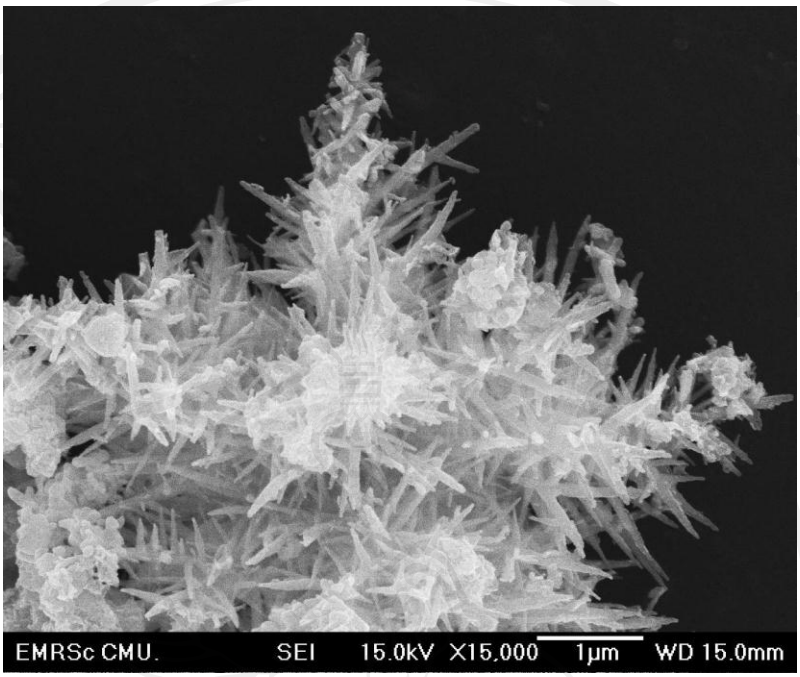

Figure 3.4 SEM image of Cu_3BiS_3 synthesized under condition of microwave power 600 W, 40 cycles.

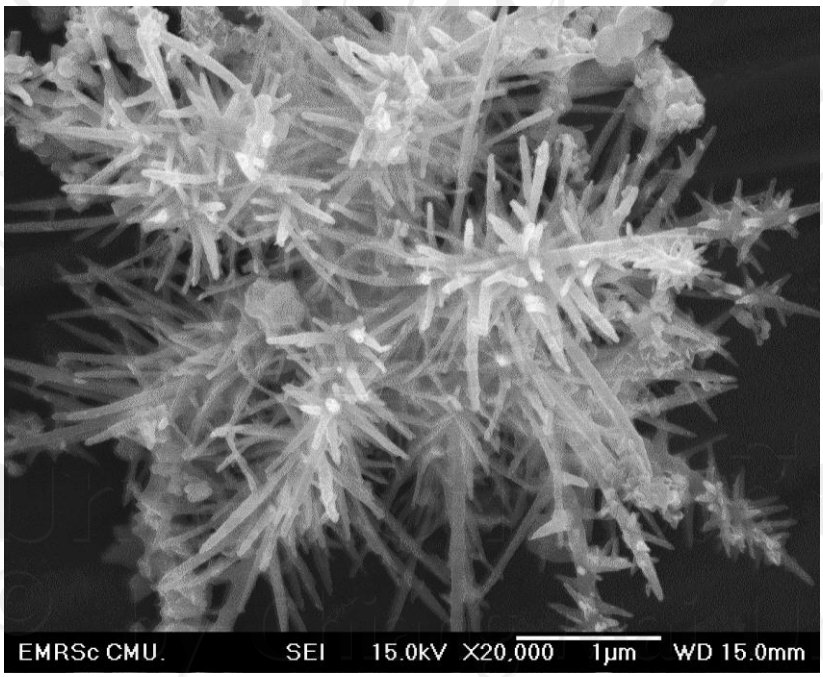

Figure 3.5 SEM image of Cu_3BiS_3 synthesized under condition of microwave power 700 W, 40 cycles.

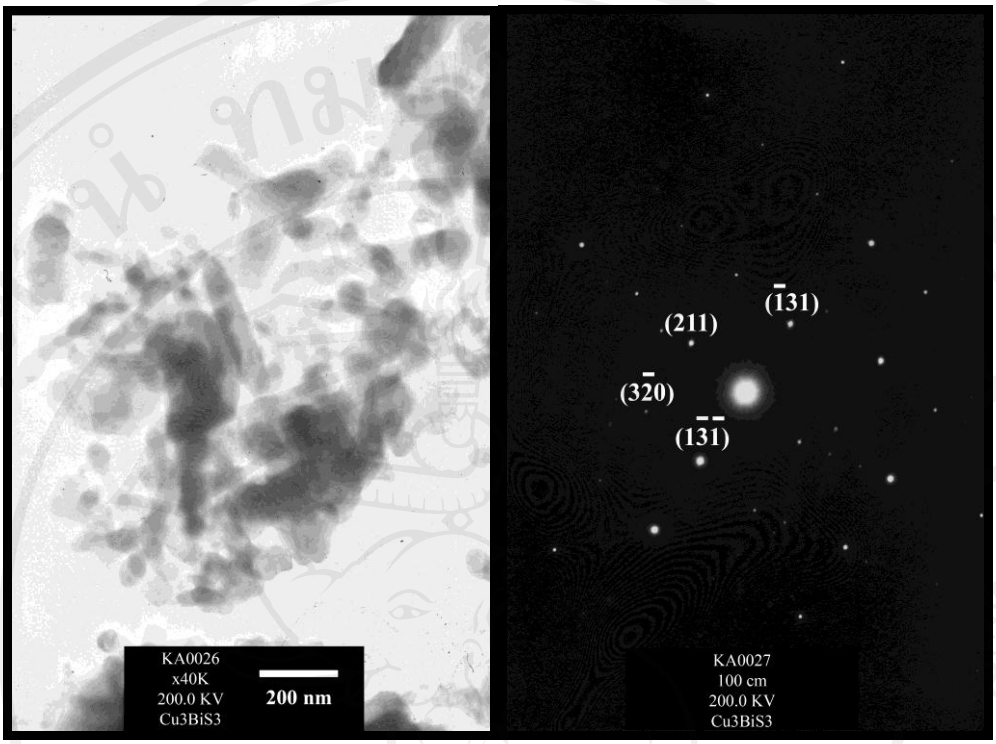

Figure 3.6 TEM image (right) and SAED pattern (left) of Cu_3BiS_3 synthesized under microwave radiation 40 cycles, microwave power 300 W.

Table 3.3 The spot diffraction pattern values of Cu_3BiS_3 produced under microwave radiation 40 cycles, microwave power 300 W

Spot	Radius (R) (mm)	d = L*λ/R (Å) (calculated)	d (Å) (JCPDS file No. 43-1479)	(hkl)
1	7.0	3.566	3.3550	131
2	8.75	2.852	2.8580	211
3	11.0	2.269	2.2735	320

On increasing microwave power to 450 W, the small dendrite-like structure was obtained (Figure 3.7 right). From the image, dendrites were sprit into differential orientation. The SAED pattern of the products synthesized using 300 and 450 W clearly indicated that the products were polycrystalline of Cu_3BiS_3 (Figure 3.6-3.7 left). The spot and diffraction concentric rings patterns were indexed to orthorhombic Cu_3BiS_3 (JCPDS No. 43-1479). No Cu_2S impurity was detected in the SAED pattern of the product synthesized at 300 and 450 W, due to the very low Cu_2S concentration in this host sample. The spot and ring diffraction pattern information which was utilized for calculating interplanar spacing and miller index of each atomic plane in Cu_3BiS_3 crystal lattice are shown in Table 3.3-3.4.

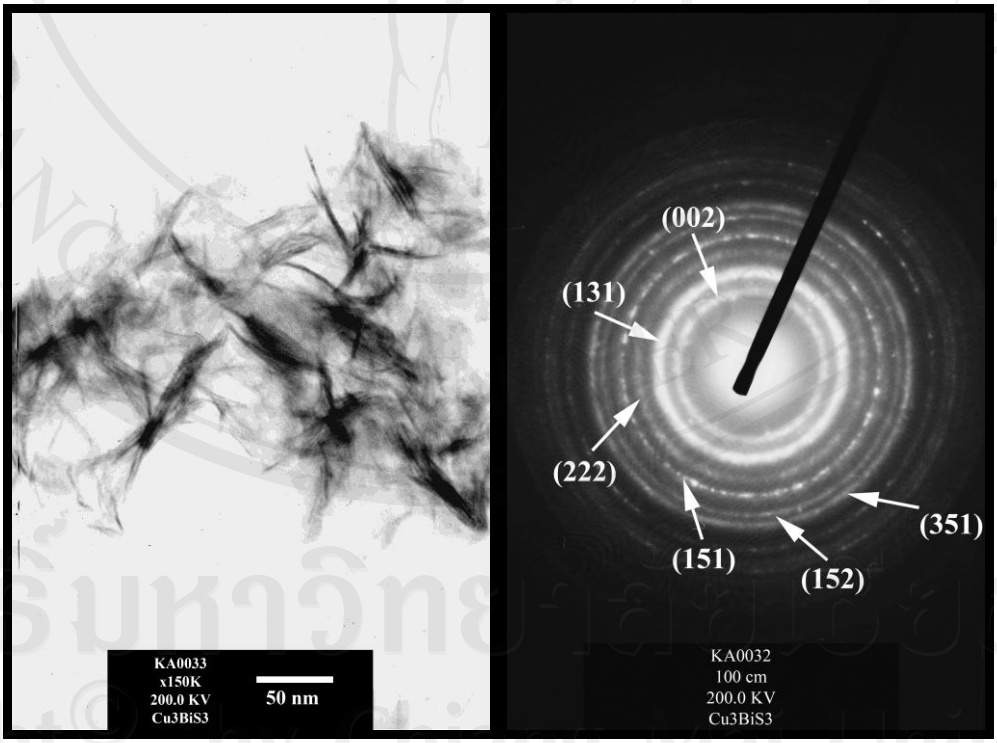

Figure 3.7 TEM image (right) and SAED pattern (left) of Cu_3BiS_3 synthesized under microwave radiation 40 cycles, microwave power 450 W.

Table 3.4 The ring diffraction pattern values of Cu_3BiS_3 produced under microwave radiation 40 cycles, microwave power 450 W

Ring No.	Diameter (mm)	Radius (R) (mm)	d = L*λ/R (Å) (calculated)	d (Å) (JCPDS file No. 43-1479)	(hkl)
1	14.0	7.0	3.566	3.3550	002
2	17.5	8.75	2.852	2.8580	131
3	22.0	11.0	2.269	2.2735	222
4	26.0	13.0	1.920	1.9213	151
5	29.5	14.75	1.695	1.6953	152
6	31.8	15.9	1.570	1.5701	351

When using higher microwave power to 600 W, the TEM image (Figure 3.8 right) of this product confirms that the dendrite structures were larger than that synthesized in the lower microwave power. TEM image of a segment of the dendrite-like structure synthesized under microwave power 700 W is shown in Figure 3.9, which is in good agreement with that obtained from SEM observation mentioned before. The whole product consisted of dendrites with different orientations. This phenomenon proved that microwave radiation at higher powers has a strong influence on vibrating atoms to form a crystal lattice, and that orthorhombic Cu_3BiS_3 unit cells were able to arrange themselves to fit with both nanoparticles and dendrites.

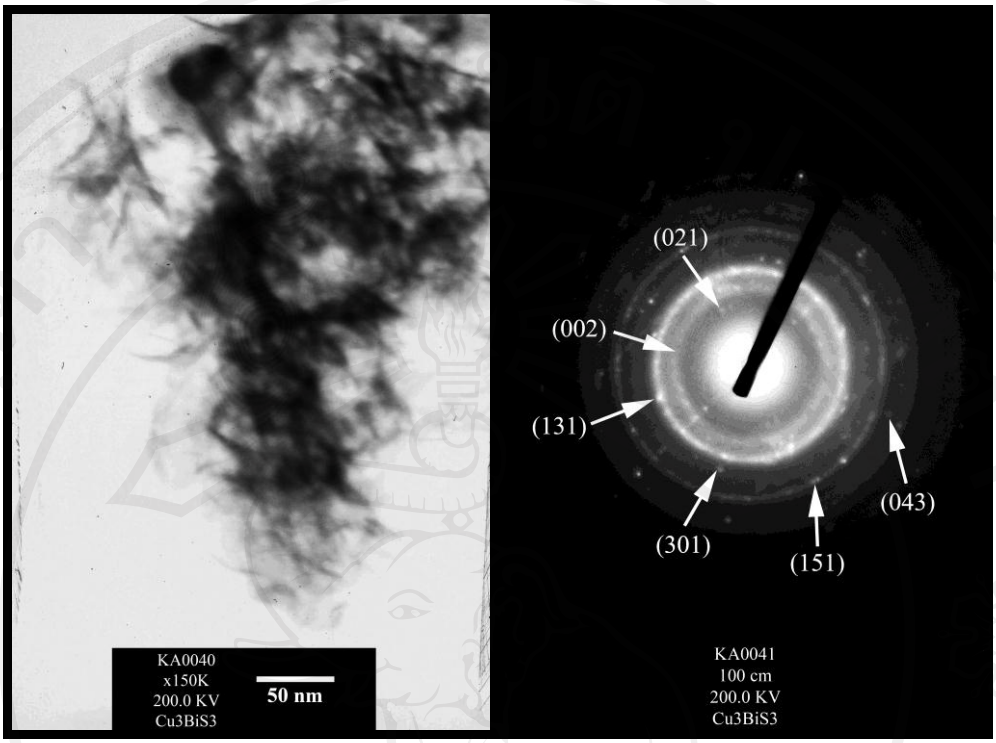

Figure 3.8 TEM images (right) and SAED pattern (left) of Cu_3BiS_3 synthesized under microwave irradiation 40 cycles, microwave power 600 W.

Table 3.5 Ring diffraction pattern values of Cu_3BiS_3 produced under microwave radiation 40 cycles, microwave power 600 W

Ring No.	Diameter (mm)	Radius (mm)	d = L*λ/R (Å) (calculated)	d (Å) (JCPDS file No. 43-1479)	(hkl)
1	12.0	6.0	4.160	4.1110	021
2	15.0	7.5	3.328	3.3550	002
3	17.5	8.75	2.852	2.8580	131
4	20.8	10.4	2.400	2.3961	301
5	26.0	13.0	1.920	1.9213	151
6	29.5	14.75	1.692	1.6953	043

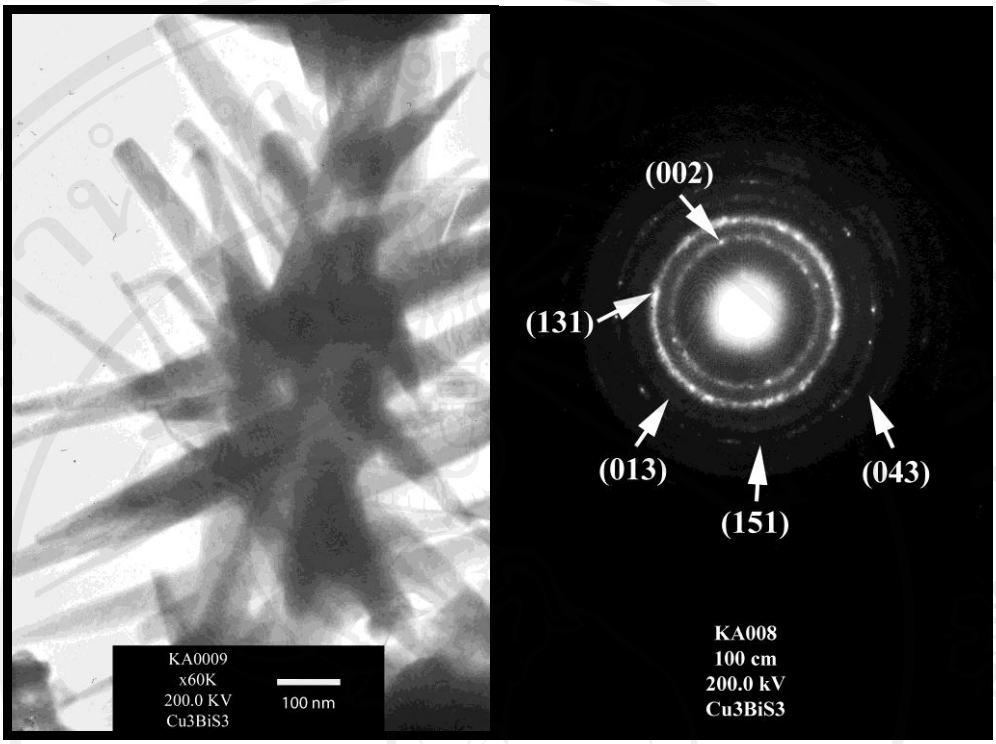

Figure 3.9 TEM images (right) and SAED pattern (left) of Cu_3BiS_3 synthesized under microwave irradiation 40 cycles, microwave power 700 W.

Table 3.6 Ring diffraction pattern values of Cu_3BiS_3 produced under microwave radiation 40 cycles, microwave power 700W

Ring No.	Diameter (mm)	Radius (R) (mm)	d = L*λ/R (Å) (calculated)	d (Å) (JCPDS file No. 43-1479)	(hkl)
1	14.0	7.0	3.566	3.3550	002
2	17.5	8.75	2.852	2.8580	131
3	23.0	11.5	2.170	2.1867	013
4	26.0	13.0	1.920	1.9213	151
5	29.5	14.75	1.695	1.6953	043

SAED patterns of the whole products, synthesized using 600, and 700 W appear as concentric rings of bright spots of polycrystals but that of a dendrite synthesized at 700 W (Figure 3.9 left) was composed of systematic spots of diffraction electrons from a single crystal. The patterns for both polycrystals and single crystal were interpreted [83], and specified as orthorhombic Cu_3BiS_3, with the electron beam for the interpretation of Figure 3.9 (left) in the $[4\bar{3}\bar{5}]$ direction. The SAED pattern recorded from the part of an individual segment (Figure 3.10 top right), the (211), $(1\bar{2}2)$, $(13\bar{1})$ and $(\bar{1}\,\bar{3}1)$ planes are determined from the sharp spot. It is confirmed that theCu_3BiS_3dendrite are polycrystal and each individual segment is a single crystal. An electron diffraction pattern was also simulated (Figure 3.10 top left) [84], using the $[4\bar{3}\bar{5}]$ direction as a zone axis. It appears as a systematic array of spots, corresponding to that obtained by the interpretation of Figure 3.10 (top right) – showing that this electron diffraction pattern of the product could exist in reality. When a dendrite, produced at 700 W, was characterized using HRTEM (Figure 3.10 bottom), a number of the (011) planes 5.6 Å apart were detected – implying that the dendrite was single crystal of the orthorhombic Cu_3BiS_3.

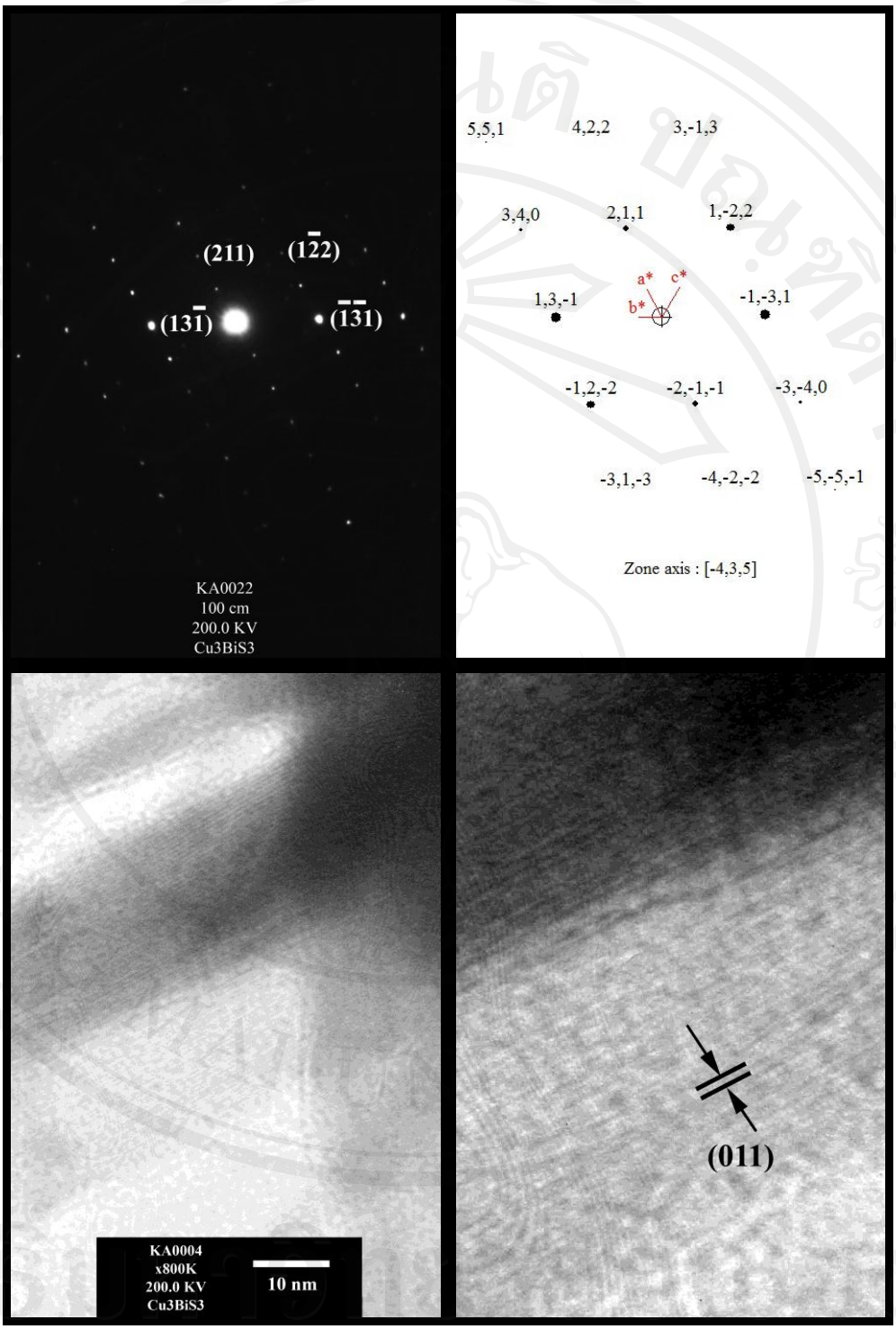

Figure 3.10 SAED pattern (top right), simulated SAED pattern (top left) and HRTEM images (bottom) of Cu_3BiS_3 synthesized under microwave irradiation 40 cycles, microwave power 700 W.

In this research, CuCl and $BiCl_3$ were dissolved in ethylene glycol to form a solution. L-cysteine, a genetically coded amino acid, was used as a sulfur source and complexing agent. By adding L-cysteine to the solution, Cu^+ and Bi^{3+} ions coordinated with it to form complexes.

$$Cu^+ + \text{L-cysteine} \xrightarrow{coordination} [Cu(\text{L-cysteine}) \text{ complexes}]$$

$$Bi^{3+} + \text{L-cysteine} \xrightarrow{coordination} [Bi(\text{L-cysteine}) \text{ complexes}]$$

Under 700 W CMR, these complexes decomposed, and Cu_3BiS_3 nuclei were synthesized very rapidly. At this stage, the number of free ions was very low. Thus, Cu_2S and Bi_2S_3 formations were inhibited [52, 85].

Concurrently, [Cu-Bi(L-cysteine) complexes] could possibly form by the reaction

$$Cu^+ + Bi^{3+} + \text{L-cysteine} \xrightarrow{coordination} [\text{Cu-Bi(L-cysteine) complexes}]$$

These complexes were then decomposed by cyclic microwave radiation.

$$[\text{Cu-Bi(L-cysteine) complexes}] \xrightarrow{decomposition} Cu_3BiS_3(\text{nuclei})$$

These nuclei grew to synthesize Cu_3BiS_3 dendrites. Dendritic growth was promoted by the strong atomic vibrations. Thus these atoms had more chances to arrange themselves in perfect order to form dendritic crystals. In the present research, cyclic microwave radiation played a key role in the growth of Cu_3BiS_3 crystals: both in the decomposition of the complexes, and in the nucleation and growth of Cu_3BiS_3.

By using cyclic microwave radiation synthesis, the process is rapid and homogenous, providing a uniform growth environment; thus crystalline dendrites were rapidly synthesized. At 300 W cyclic microwave radiation, the nucleation rate of Cu_3BiS_3 was slower; Cu_2S at very low concentration thus had a better chance to nucleate as a second phase contained in this nanoparticles product.

Photoluminescence (PL) of Cu_3BiS_3 dendrites was studied at room temperature, using 300 nm excitation wavelength of a xenon laser. The spectrum (Figure 3.11) was blue emission centered at 367 nm, with the shoulder at 412 nm which is caused by some defects that originated during the synthesis process.

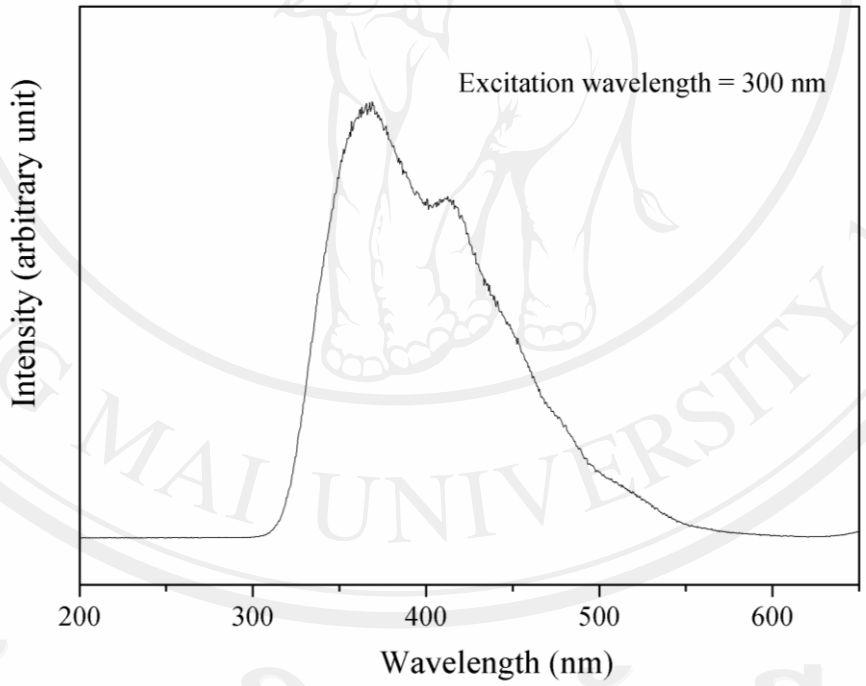

Figure 3.11 PL emission of Cu_3BiS_3 dendrites synthesized at 700 W.

The PL spectrum is in agreement with the J. Zhong et al. work [41] which was found that there were 2 distinct emission peaks observed in PL study of Cu_3BiS_3 semiconductor.

The optical characteristics were measured and show a plot of $(\alpha h\nu)^2$ against $h\nu$ in Figure 3.12. The nature and magnitude of the optical band gap may be determined from the fact that $\alpha h\nu$ is proportional to $(h\nu - Eg)^n$. As a consequence, plot of $(\alpha h\nu)^{1/n}$ against $h\nu$, with $1/n$ = 2, 2/3, 1/2, 1/3, for direct, direct forbidden, indirect, and indirect forbidden, respectively, are linear, with the intercept yielding the value of the band gap. Plot in Figure 3.12 is $(\alpha h\nu)^2$ as a function of energy, the linear plot identifies the band gap as direct, and intercept gives the magnitude of the band gap energy (E_g) as 1.56 eV. The energy band gap of as-synthesized Cu_3BiS_3 powder was slightly larger than E_g of thin film Cu_3BiS_3 which was reported at 1.2-1.4 eV [13, 35]. The energy band gap is gradually increased for the smaller sized particles because the gap between the valence and the conduction bands increases with the decreasing particle size by comparing with the bulk materials which the valence band is closed to conduction bands.

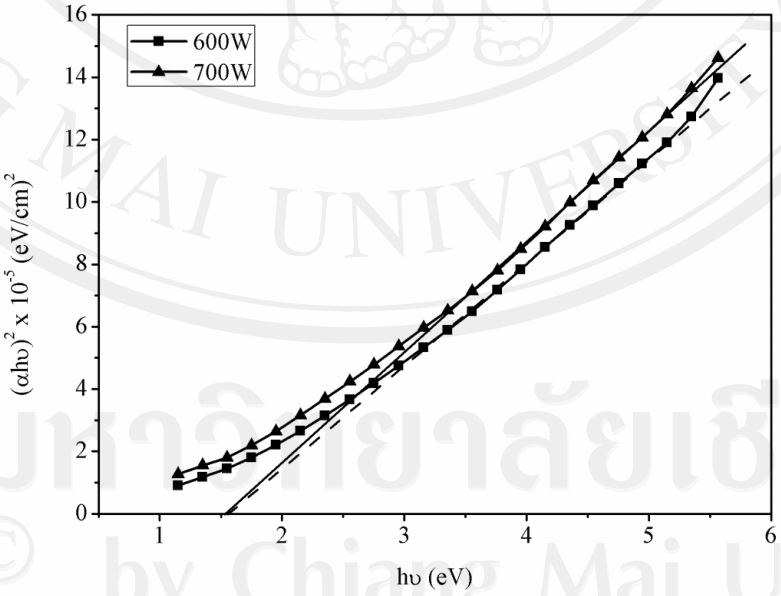

Figure 3.12 The band gap energy of the Cu_3BiS_3 prepared at microwave power 600 W and 700 W.

3.2 Characterization of Cu_3SbS_4 microflowers produced by a cyclic microwave radiation

XRD patterns (Figure 3.13) of the products, produced using various molar ratios of Cu:Sb:S, were compared with the JCPDS database No. 10–0472 (Cu_3SbS_4), 02–1284 (Cu_2S), and 71–2432 (Sb_2S_3) [81]. Both Cu_3SbS_4 and Cu_2S impurity were detected in the CSbS1, CSbS2, CSbS3, and CuSbS4 products, due to the excess amount of Cu^+ and S^{2-}. When adding excess amount of Cu^+ and S^{2-} was employed, reaction of some Cu^+ with S^{2-} could have been accompanied with formation of Cu_3SbS_4 major phase which result in the mix phases in the final products. For 3:3:4 (CSbS5) and 2:2:4 (CSbS7) molar ratios of Cu:Sb:S, pure tetragonal Cu_3SbS_4 was detected. Adding equal amount of Cu^+ : Sb^{3+} could prevent the formation of impurity such as Cu_2S or Sb_2S_3 in the final products. In these two conditions, some Sb^{3+} and sulfur were likely to be left in the products, and washed out by ethanol. But for the 1:1:4 molar ratio Cu:Sb:S (sample CSbS8), Cu_3SbS_4 product and Sb_2S_3 impurity were detected which caused by the reaction of remaining Sb^{3+} with the excessive amount of S^{2-}.

The interplanar spacing (d) and lattice parameter (a, b, c) of Cu_3SbS_4 synthesized using 2:2:4 mole ratio of Cu:Sb:S were calculated using Bragg's law and the plane-spacing equation below, since a = b for tetragonal phase crystal [82].

$$\frac{1}{d^2} = \frac{(h^2 + k^2)}{a^2} + \frac{1}{c^2}$$

The interplanar spacings of different planes are in good accordance with those of the JCPDS standard as shown in Table 3.7 [81].

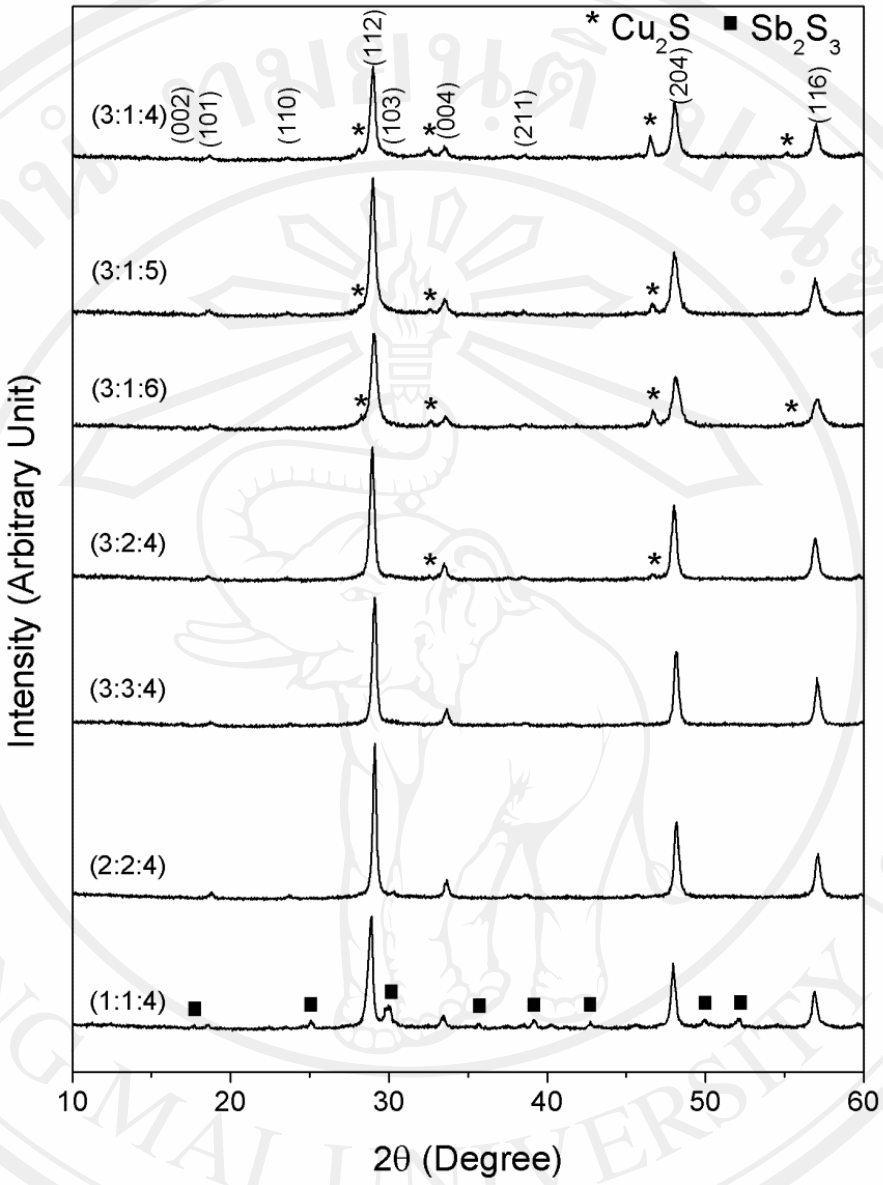

Fig. 3.13 XRD patterns of Cu_3SbS_4 produced from different molar ratios of Cu:Sb:S in40 ml ethylene glycol by 300W cyclic microwave radiation for 40 cycles.

Table 3.7 The 2θ diffraction angles and intensities of the JCPDS no. 10-0472 and the data of Cu_3SbS_4 (synthesized at 2:2:4 mole ratio of Cu:Sb:S) obtained from the experiment

Plane	JCPDS		Experiment	
	2θ (deg.)	Relative Intensity (%)	2θ (deg.)	Relative Intensity (%)
101	18.745	30	18.79	3.31
110	23.695	10	23.73	2.05
112	29.053	100	29.11	100.00
103	30.252	20	30.29	2.87
004	33.614	50	33.65	11.68
211	38.507	30	38.61	1.58
204	47.969	80	48.13	48.75
116	57.013	70	57.13	28.10

Table 3.8 Calculated lattice parameter of Cu_3SbS_4 from the experiment (synthesized at 2:2:4 mole ratio of Cu:Sb:S), comparing with the JCPDS file (Reference code: 10-0472)

Plane	2θ (degree)		Interplanar spacing (d), Å		Lattice parameter, Å	
	Exp.	JCPDS file	Exp.	JCPDS file	Exp.	JCPDS file
004	33.65	33.614	2.661	2.6640	c = 10.44	c = 10.7600
110	23.73	23.695	3.746	3.7520	a = b = 5.30	a = b = 5.3800

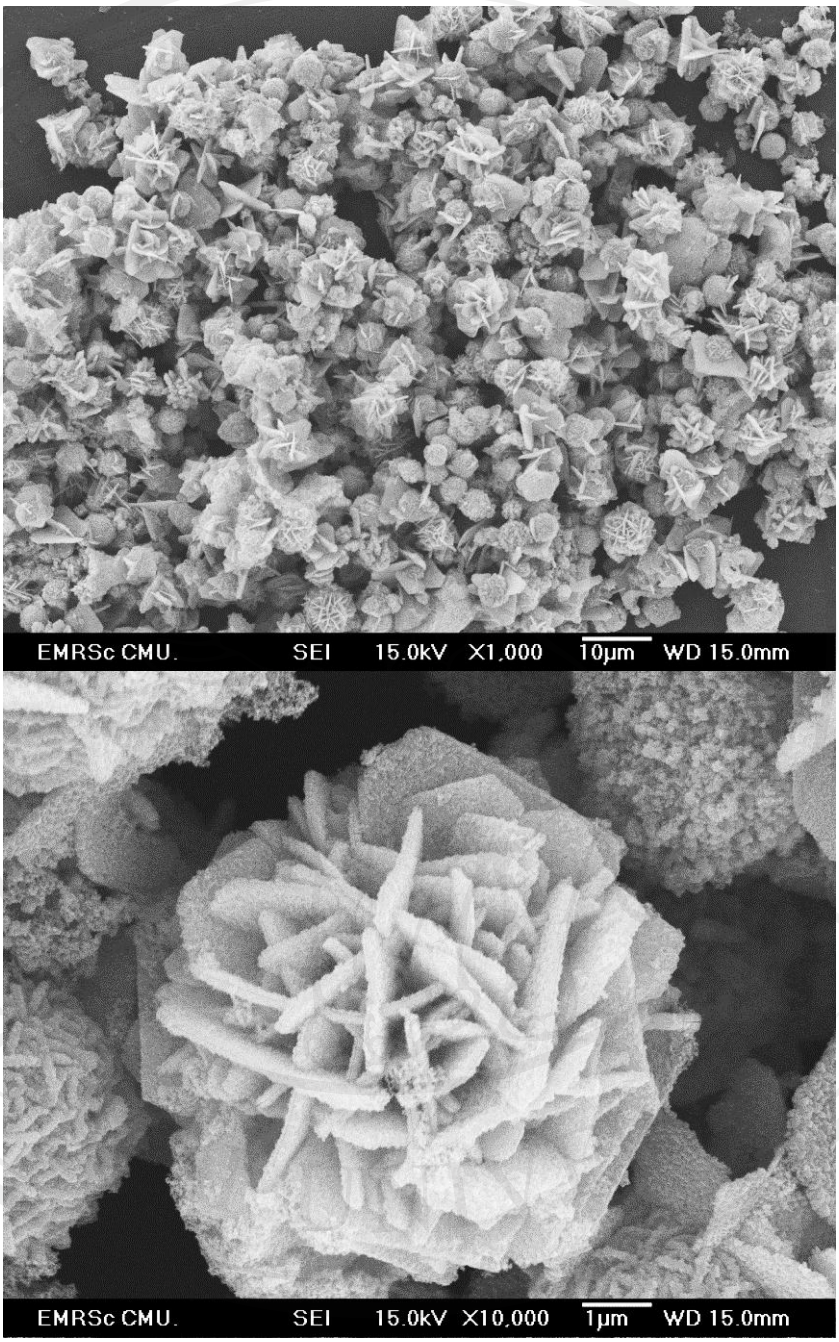

Figure 3.14 (upper) SEM images of Cu_3SbS_4 synthesized at 2:2:4 molar ratio of Cu:Sb:S, and (lower) high magnificent SEM images of the product.

Figure 3.14 (upper) show typical images of the Cu_3SbS_4 black powder produced from 2:2:4 molar ratios of Cu:Sb:S in 40 ml ethylene glycol by a 300W cyclic microwave radiation for 40 cycles. This product was Cu_3SbS_4 microflowers with their petals formed by clustering of different particles (Figure 3.14 lower).

EDX analysis (Fig. 3.15) revealed the presence of Cu, Sb, and S as the fundamental elements of these flowers, including sputtered Au to improve the conductivity for SEM analysis. The composition of product was examined by EDX as shown in Table 3.9, the ratio of Cu:Sb:S is approximately 37.3 : 16.8 : 45.8 or 2.2 : 1 : 2.7 which is slightly different from the stoichiometric ratio of Cu_3SbS_4 (Cu:Sb:S = 3:1:4). The excess atomic ratio of Sb ion in the EDX analysis could be come from incompletely washed out of Sb^{3+} reactant.

Table 3.9 Measured composition of Cu_3SbS_4 by EDX analysis produced by using 2:2:4 molar ratio Cu:Sb:S in 40 ml ethylene glycol

Element	Weight%	Atomic%
S K	24.97	45.86
Cu K	40.26	37.32
Sb L	34.77	16.82
Totals	100.00	

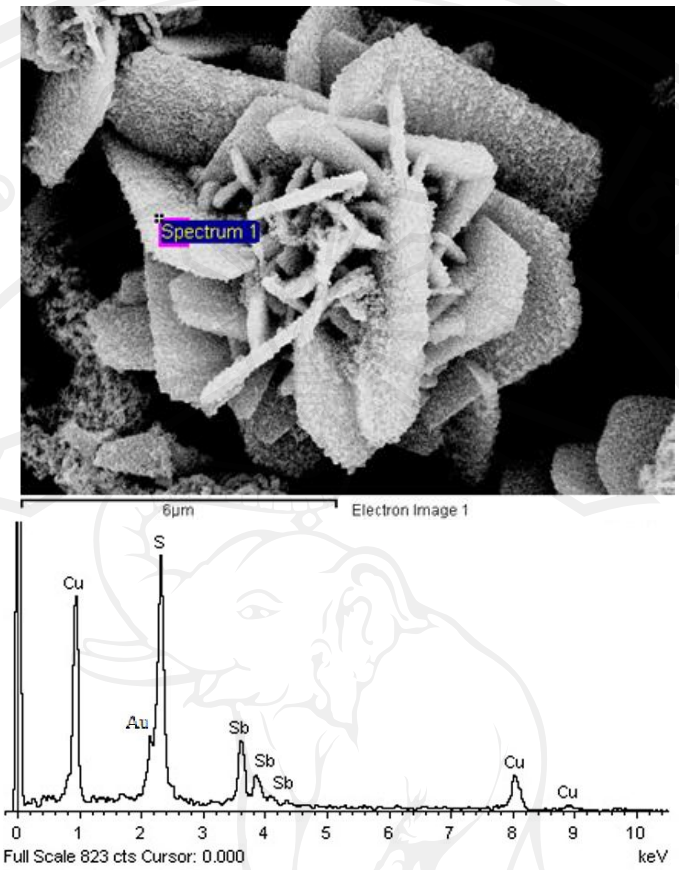

Figure 3.15 An analytic area of the product (upper) and EDX analysis (lower) of Cu_3SbS_4 produced by using 2:2:4 molar ratio Cu:Sb:S in 40 ml ethylene glycol.

Upon increasing the Cu:Sb:S molar ratio from 2:2:4 to 3:3:4 in 40 ml ethylene glycol, the product became clusters of irregular particles with different orientations (Figure 3.16) which caused by the limited space for their growth. At 3:3:4 molar ratios (CSbS5), the sample was the solution with higher concentration than sample CSbS7 (2:2:4 molar ratios). Thus, there is lower space for Cu^{+}, Sb^{3+} ions or S source to move easily and the growth of crystal into microflower morphology was restrained. By adding ethylene glycol until its content was 60 ml (Figure 3.17), sample CSbS6, different flower-like particles were reproduced.

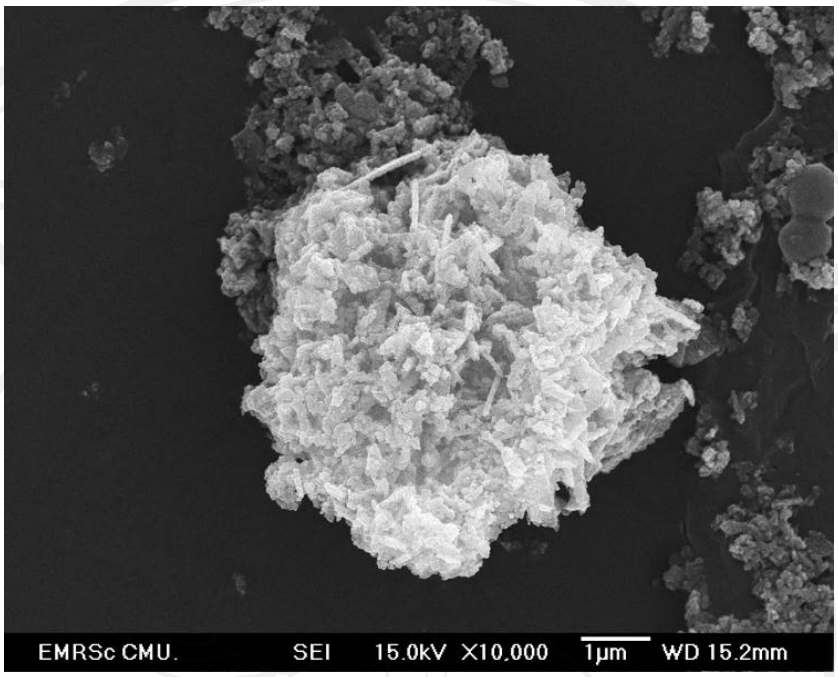

Figure 3.16 SEM image of Cu_3SbS_4 synthesized at 3:3:4 molarratio Cu:Sb:S in 40 ml ethylene glycol.

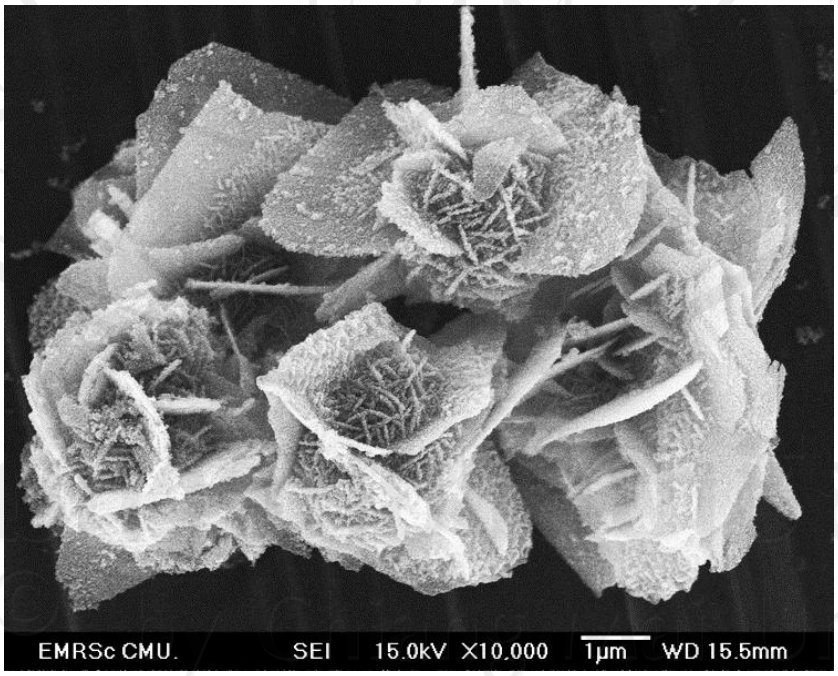

Figure 3.17 SEM image of Cu_3SbS_4 synthesized at 3:3:4 molarratio Cu:Sb:S in 60 ml ethylene glycol.

It is very interesting that concentration of synthesized solution has effect on morphology of as-prepared product. At lower concentration, 60 ml of ethylene glycol solution, there is larger space for Cu^{+}, Sb^{3+} ions or S source to move easily. As a result, the reagent at this state could form the Cu_3SbS_4 structure in larger size. This phenomenon justified the influence of the solution concentration on the growth of crystal during the synthesis reaction.

Upon lowering the processing time of the CSbS7 mixture from 40 cycles to 30, 20, and 10 cycles, the products (Figure 3.18 a-f) produced from 2:2:4 molar ratio Cu:Sb:S remained as black microflowers with reducing sizes in sequence. That means increasing of operation cycles leaded to growing of Cu_3SbS_4 microflower from small microflower with flat petals to be larger microflower with rough petals formed by clustering of different particles. Until for 2 cycles, the white precipitate-product (Figure 3.18 g and h) was rectangular sticks, showed that reagents had formed white complexing agent of metal-thiourea. When the sample of solution was irradiated for longer processing time by microwave radiation, the heat is generated in the solution leads to breaking down of unstable metal-thiourea complex. After that, The Cu^{+}, Sb^{3+} and S^{2-} can rearrange themselves to grow into black powder of Cu_3SbS_4 crystallite with microflower morphology. These results are in according with the XRD results in which adding excess amount of metal and sulfur source caused the CuS or Sb_2S_3 impurities in the final product due to there were large amount of metal-complex occurred in the solution at the earlier state of microwave radiation process.

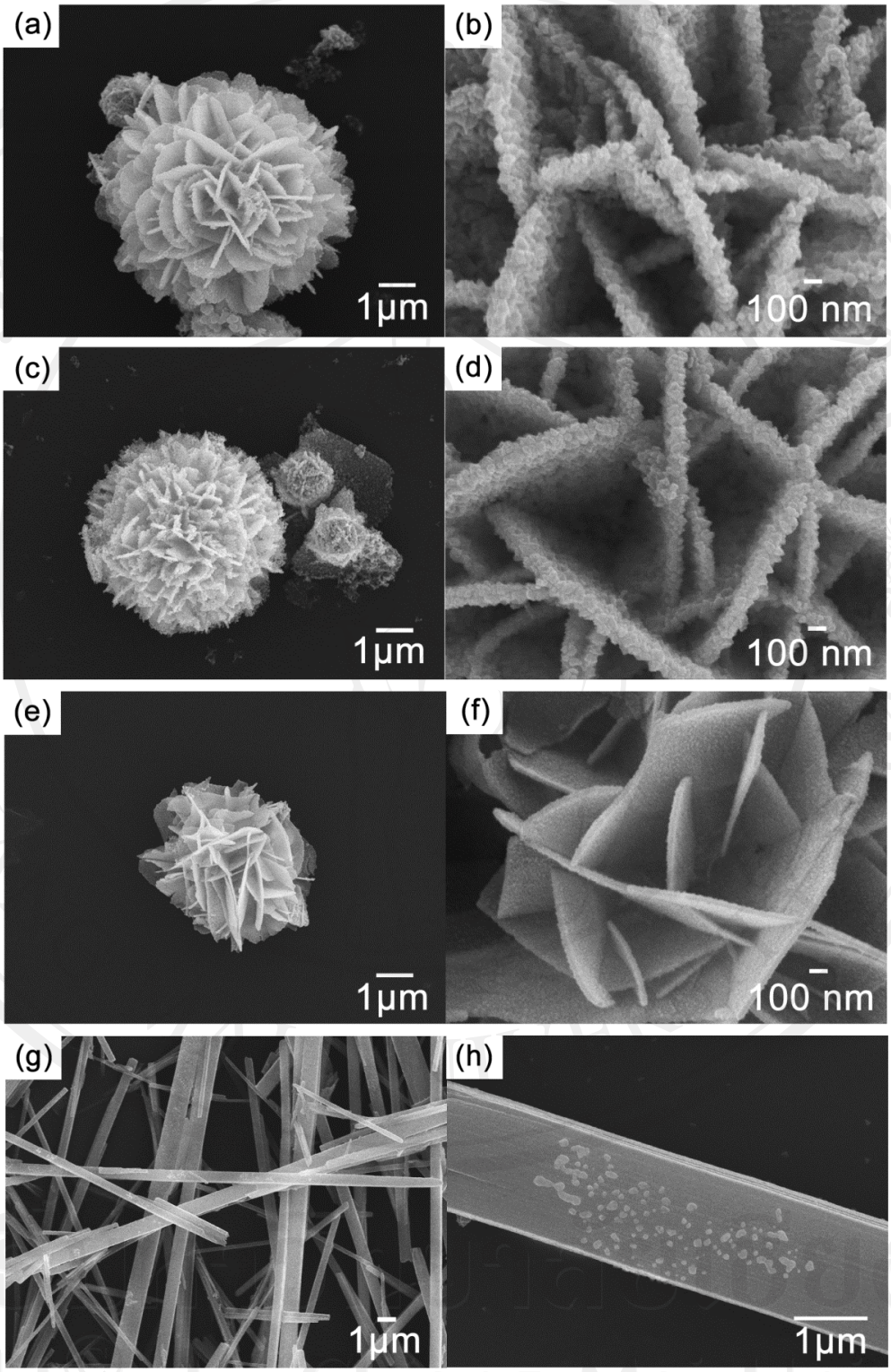

Figure 3.18 SEM images of Cu_3SbS_4 produced from 2:2:4 molar ratio Cu:Sb:S in 40 ml ethylene glycol by 300 W cyclic microwave radiation for (a, b) 30, (c,d) 20, (e,f) 10 and (g-h) 2 cycles.

For possible formation mechanism of producing of Cu_3SbS_4, CuCl+Thiourea and $SbCl_3$+Thiourea solutions were mixed. Thus complexes were possibly formed.

$$Cu^{+} + \text{Thiourea} \xrightarrow{coordination} [Cu(\text{Thiourea}) \text{ complexes}]$$

$$Sb^{3+} + \text{Thiourea} \xrightarrow{coordination} [Sb(\text{Thiourea}) \text{ complexes}]$$

These complexes were mixed, and processed by a cyclic microwave radiation to produce Cu_3SbS_4.

$$[\text{Cu-TU complexes}] + [\text{Sb-TU complexes}] \xrightarrow{coordination} Cu_3SbS_4 \text{ (nuclei)}$$

Alternatively, Cu-Sb-TU complexes could also form.

$$Cu^{+} + Sb^{3+} + TU \xrightarrow{coordination} [\text{Cu-Sb-TU complexes}]$$

And Cu_3SbS_4 nuclei were produced by cyclic microwave radiation.

$$[\text{Cu-Sb-TU complexes}] \xrightarrow{coordination} Cu_3SbS_4 \text{ (nuclei)}$$

During processing for 10–40 cycles, the nuclei grew to form pure nanostructured flowers (CSbS7 mixture).When the contents of Cu^{+} and S^{2-} were excessive, Cu_2S impurity was produced. Sb_2S_3 could also form, due to the excess of Sb^{3+} and S^{2-}.

Further information about Cu_3SbS_4 microflower product produced from 2:2:4 molar ratios of Cu:Sb:S was obtained from transmission electron microscopy (TEM). TEM and HRTEM images (Figure 3.19a-c) further confirm that the petals of

microflower are constructed by clustering of abundant nanoparticles array in different direction and each nanoparticle is single crystalline with randomly crystal plane, for example (110), (103) lattice planes. Upon increasing the molar ratio from 2:2:4 to 3:3:4, the product became clusters of irregular nanoparticles with different orientations (Figure 3.19f).

For the product produced from 2:2:4 molar ratio Cu:Sb:S in 40 ml ethylene glycol, the SAED pattern (Figure 3.19d) was interpreted [83] and specified as tetragonal Cu_3SbS_4[81]. It was in good accordance with that obtained by simulation (Figure 3.19e) [84], although some spots of the interpreted pattern did not appear on the simulated one – due to the following. To simulate the pattern, intensity and size of the spots (planes) were mutually related. The stronger intensity was used, the larger size was achieved. The intensity and size of the spots were limited by a saturated intensity used for simulation. Thus some planes of the JCPDS database with low intensity did not appear in the simulated pattern. A SAED pattern (Figure 3.19g) of the product produced from 3:3:4 molar ratio Cu:Sb:S was composed of bright spots of diffuse concentric rings, specified as polynanocrystalline Cu_3SbS_4.

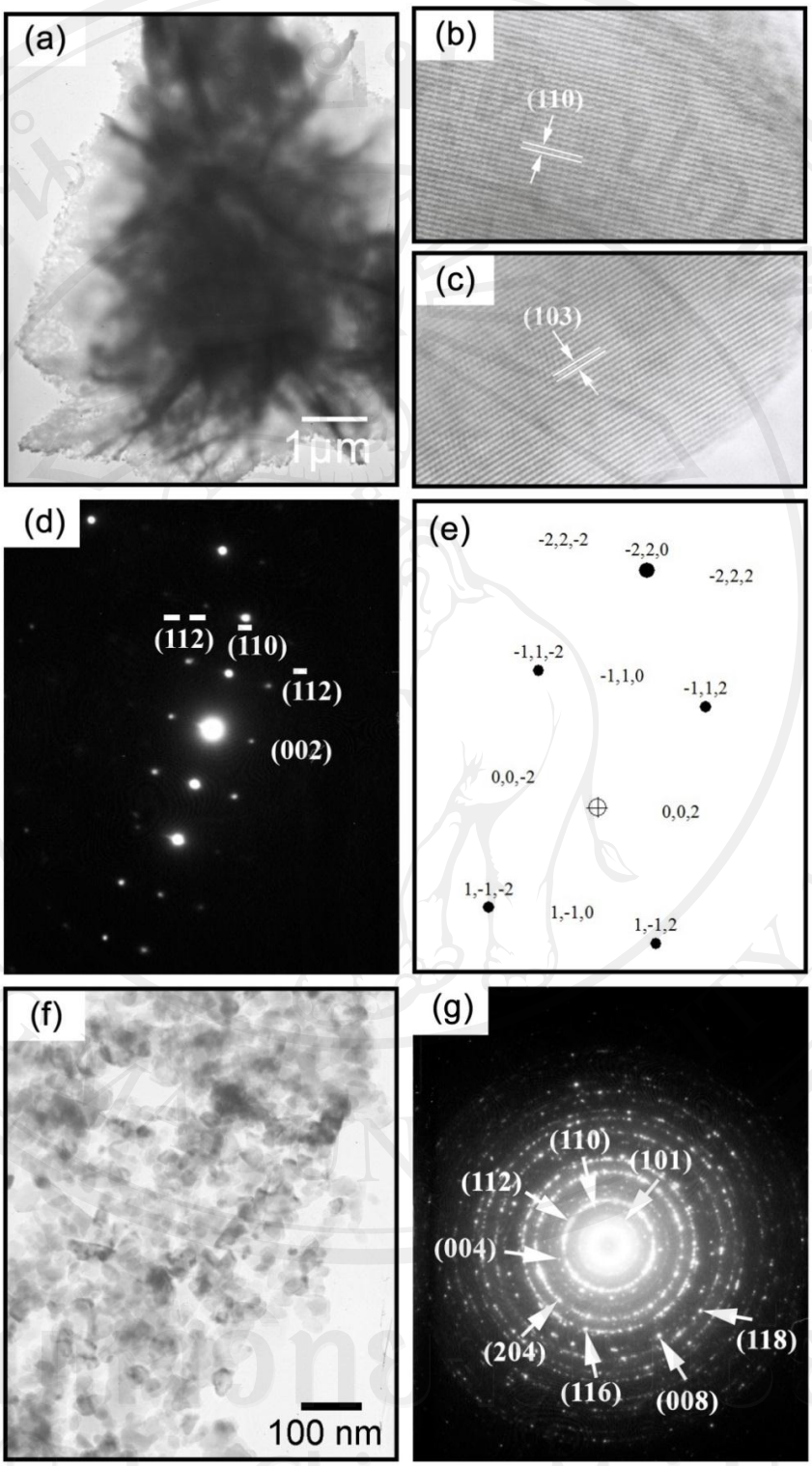

Figure 3.19 TEM and HRTEM images, and SAED and simulated patterns of Cu_3SbS_4 produced by 300 W cyclic microwave radiation for 40 cycles. (a-e) 2:2:4, and (f, g) 3:3:4 molar ratios of Cu:Sb:S in 40 ml ethylene glycol.

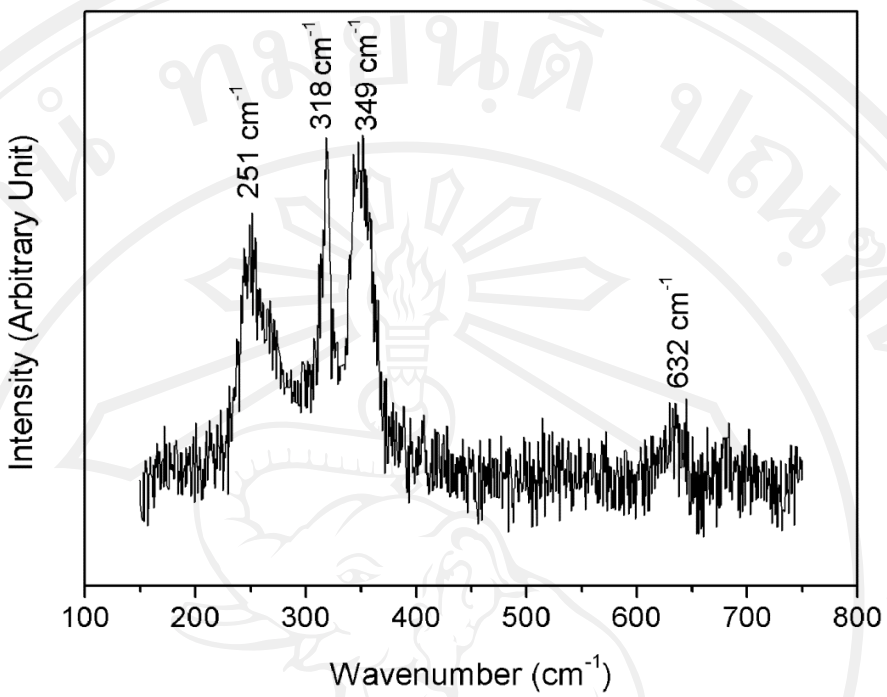

Figure 3.20 Raman shifts of Cu_3SbS_4 produced from 2:2:4 molar ratio Cu:Sb:S in 40 ml ethylene glycol by 300W cyclic microwave radiation for 40 cycles.

By using 50 mWAr green laser (514.5 nm wavelength), four Raman shifts of Cu_3SbS_4 (Figure 3.20) produced from 2:2:4 molar ratio Cu:Sb:S in 40 ml ethylene glycol by 300W cyclic microwave radiation for 40 cycles were at 251, 318,349, and 632 cm^{-1} – in accordance with the previous report [86]. The 318 and 632 cm^{-1} peaks seemed to correspond with the fundamental and overtone modes, respectively. Its UV-visible absorption (Figure 3.21) was controlled by two photon energy (hν) range. For $h\nu > E_g$, the curve for direct interband transitions was linearly increased with the increasing of hν. Its inclination was caused by the absorption for charged transition from the topmost occupied state of valence band to the bottommost unoccupied state of conduction band. For $h\nu < E_g$, the curve was different from linearity, caused by

absorption relating to defects. The direct E_g, determined by extrapolating the linear portion curve to zero absorption, was 1.47 eV– a promising E_g for multiple potential applications. It was in the same range as E_g (300 K, absorption) = 1.24 eV of Cu_3AsS_4 [87], and E_g =1.4 eV of $CuSbS_2$ thin film heated at 150 °C [88].

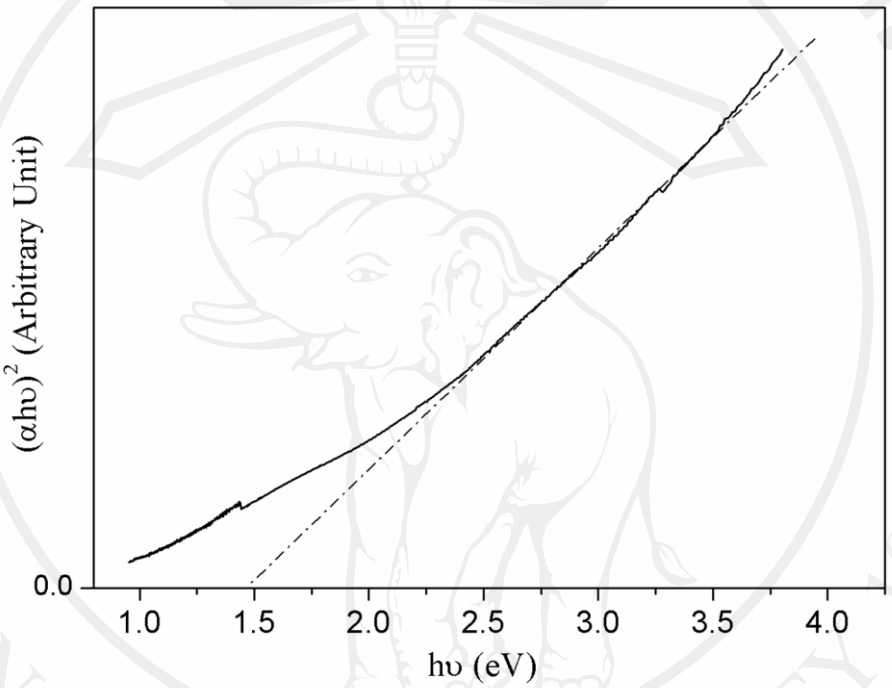

Figure 3.21 $(\alpha h\nu)^2$ versus hν plot for determination of energy gap (E_g) of Cu_3SbS_4 produced from 2:2:4 molar ratio Cu:Sb:S in 40 ml ethylene glycol by 300W cyclic microwave radiation for 40 cycles.

3.3 Cyclic microwave-assisted synthesis of $CuFeS_2$ nanoparticles using biomolecules as sources of sulfur and complexing agent

Different choices of copper precursors and iron precursors have been used for synthesis of $CuFeS_2$ nanocrystalline as shown in Table 3.10. By varying the mole ratios of copper, iron and sulfur, it was found that adding the excess amounts of iron

precursor is the optimum for synthesis of $CuFeS_2$ in order to achieve the stoichiometric composition. The crystal structure and chemical composition of the as-prepared samples were confirmed by powder X-ray diffraction. The XRD results were compared with the JCPDS database No. 01-0842 ($CuFeS_2$), 47-1748 (Cu_9S_5) and No. 75-2233 (CuS) [81]. Figure 3.22 shows the XRD patterns of all products, it is found that Cu_9S_5 product was observed in CN sample and $CuFeS_2$ major phase with CuS impurity were detected in the product using CuCl as a copper source (sample CN and sample CC). However, pure phase $CuFeS_2$ without impurity was obtained by using $Cu(CH_3COO)_2$ under the same conditions (samples CA-1 and CA-2). All diffraction peaks in the patterns are labeled and can be readily indexed to be tetragonal $CuFeS_2$. In this research by fixing the same iron sources, copper source played an important role as the precursor for the phase formation of $CuFeS_2$. It was found that $CuFeS_2$ crystals was not obtained when copper sources were not $Cu(CH_3COO)_2$.

Table 3.10 Summarized different synthesized-conditions of the samples and their products prepared by cyclic microwave radiation at 300 W with 40 cycles

Samples	**Cu-source**	**Fe-source**	**Synthesized compound**
CN	$Cu(NO_3)_2.5H_2O$	$FeCl_3.6H_2O$	Cu_9S_5
CC	CuCl	$FeCl_3.6H_2O$	$CuFeS_2$ + CuS
CA-1	$Cu(CH_3COO)_2$	$FeCl_3.6H_2O$	$CuFeS_2$
CA-2	$Cu(CH_3COO)_2$	$FeCl_2.4H_2O$	$CuFeS_2$

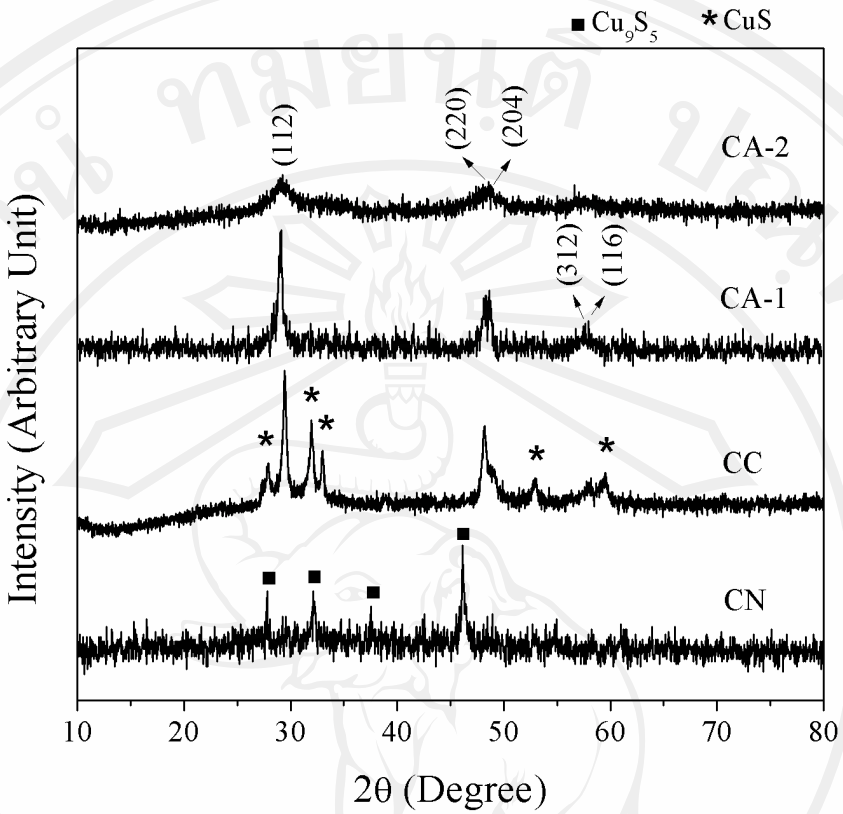

Figure 3.22 XRD patterns of samples CN, CC, CA-1 and CA-2.

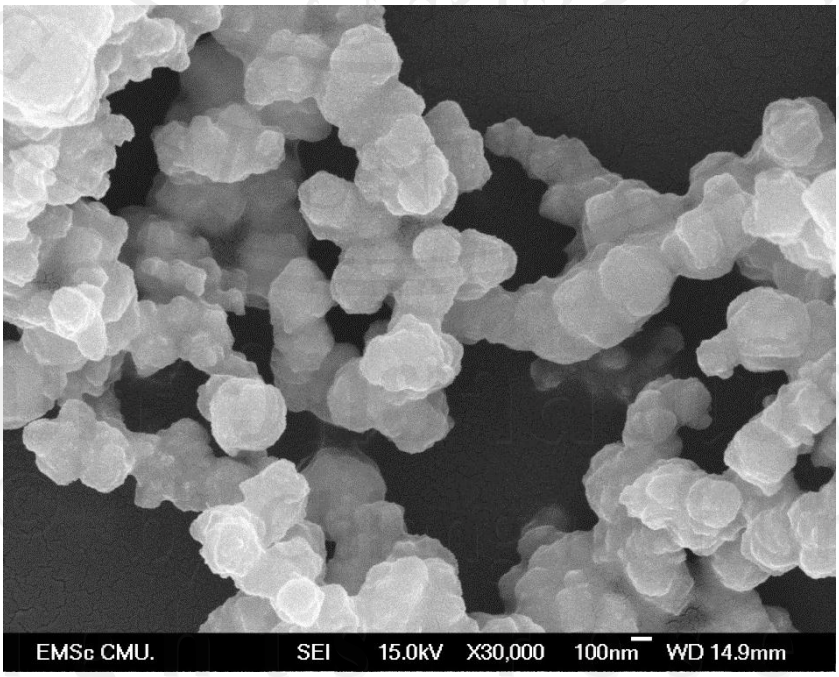

Figure 3.23 SEM images of sample CA-1 synthesized at 300W, 40 cycles.

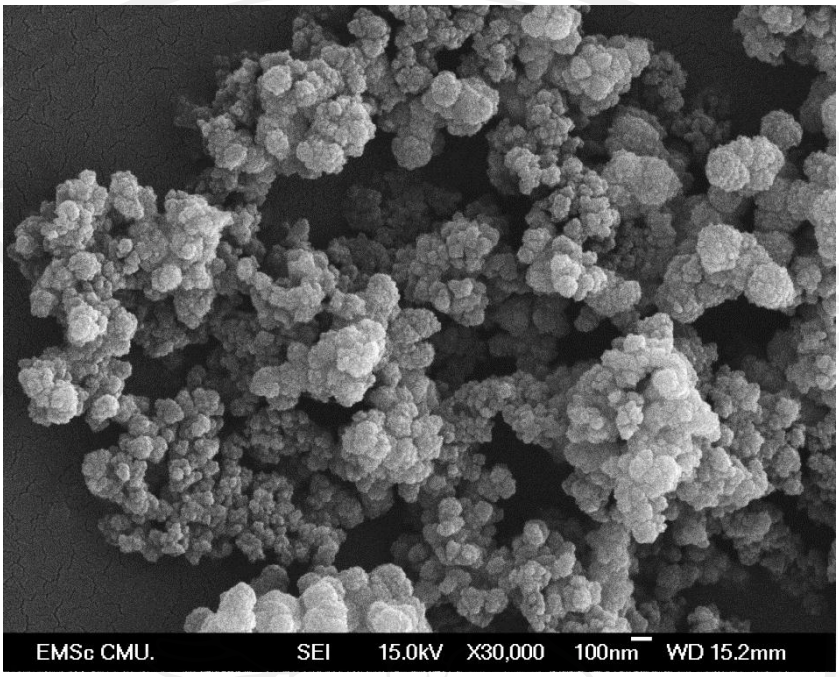

Figure 3.24 SEM images of sample CA-2 synthesized at 300W, 40 cycles

The morphology and hollow structure of samples have been determined using SEM and TEM. The effect of different iron sources on the morphology of products was also investigated. The product synthesized at 300 W 40 cycles using $Cu(CH_3COO)_2$ with $FeCl_3.6H_2O$ as precursors (Figure 3.23) exhibits the non-spherical cluster of nanoparticles. The outer surfaces of the cluster are rough, indicating that they were composed of a plenty of loosely packed nanoparticles [89]. By changing the iron source to $FeCl_2.4H_2O$, the product (Figure 3.24) became clusters of irregular nanoparticles with smaller size. EDX analysis (Figure 3.25, 3.26) revealed the presence of Cu, Fe, and S as the fundamental elements of these particles, including sputtered Au to improve the conductivity for SEM analysis, C and O due to polymer substrate. In sample CA-1, it was observed that the atomic% ratio of Cu:Fe:S is 35.01:17.35:47.64 or 2.02:1:2.7. For sample CA-2, the atomic% ratio of Cu:Fe:S is

also 33.91:21.21:44.88 or 1.5:1:2.11. There is some excess of Cu element was observed in sample CA-1 and CA-2. The excess Cu might come from the sample holder which is made from Cu metal and was used for the SEM analysis.

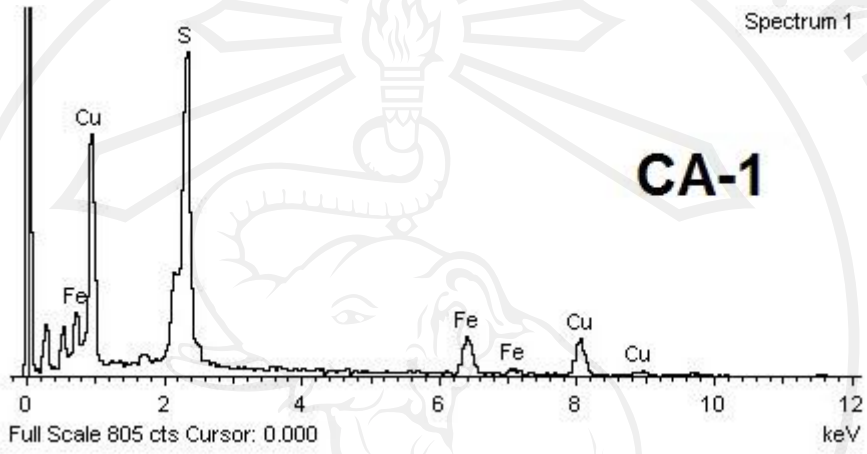

Figure 3.25 EDX spectrum of sample CA-1.

Table 3.11 Measured composition of $CuFeS_2$ (sample CA-1) by EDX analysis

Element	Weight%	Atomic%
S K	32.36	47.64
Fe K	20.52	17.35
Cu K	47.12	35.01
Totals	100.00	

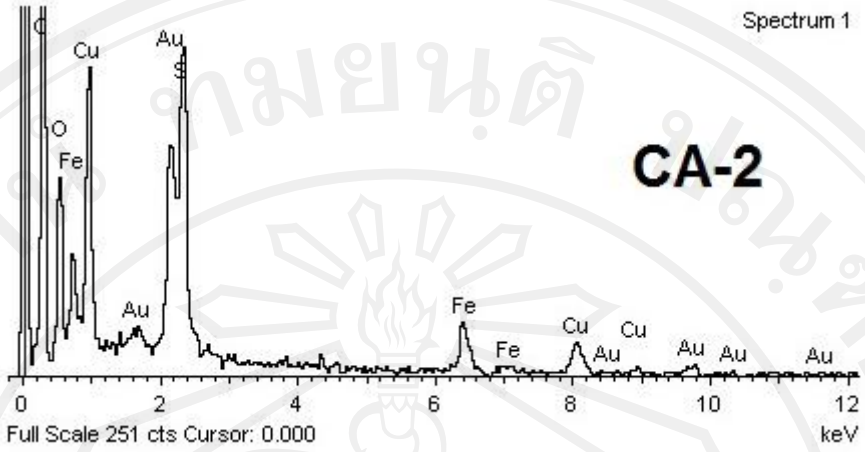

Figure 3.26 EDX spectrum of sample CA-2.

Table 3.12 Measured composition of $CuFeS_2$ (sample CA-2) by EDX analysis

Element	Weight%	Atomic%
S K	30.11	44.88
Fe K	24.79	21.21
Cu K	45.10	33.91
Totals	100.00	

The nanoparticles in cluster are further investigated by TEM images shown in Figure 3.26. The intensive contrast between the black margin and the bright center of the irregular spherical shape shows the existence of $CuFeS_2$ hollow structure in the product, which could not be observed from SEM technique. The sample CA-1 presents the hollow structure for the entire product (Figure 3.26b) which is consisted of really fine nanoparticles as seen in the magnified TEM image (Figure 3.26a). Upon

decreasing the processing time of sample CA-1 from 40 cycles to 20 and 5 cycles (Figure 3.26a-d), $CuFeS_2$ produced from $FeCl_3.6H_2O$ remained as cluster of nanoparticles, with reducing hollow structure in sequence.

The SAED patterns of all samples were composed of bright spots of diffuse concentric rings, specified as polynanocrystalline $CuFeS_2$. It is noticeable that the amount of bright concentric rings in SAED patterns of sample CA-1 produced at CMR 40, 20 and 5 cycles were gradually decreased respectively, which indicate the decrease in growth of crystal and the lesser of crystallinity in product. For sample CA-2, there are fewer numbers of the bright concentric rings in SAED pattern compare with sample CA-1. It is consistent with XRD result that sample CA-2 is lower crystalline than sample CA-1.

By changing the Fe precursor to $FeCl_2.4H_2O$ (sample CA-2), the agglomerate of nanoparticles were prepared (Figure 3.28). Development of cluster with hollow structure from very small nanoparticles could be observed in sample CA-2. The nanoparticles (Figure 3.28b) become closely as larger cluster (Figure 3.28a).

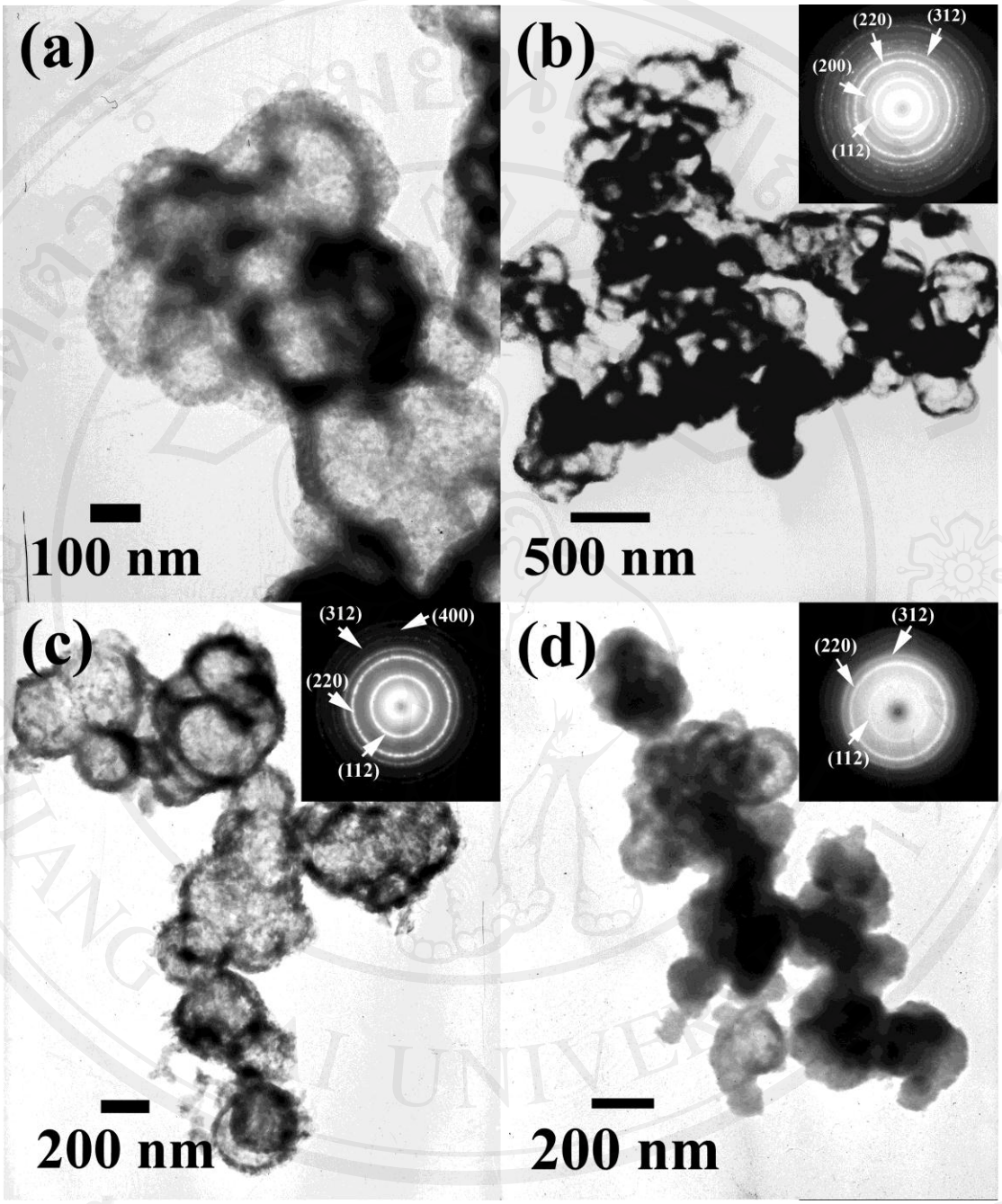

Figure 3.27 TEM images and SAED patterns of sample CA-1 synthesized at (a-b) 40 cycles of cyclic microwave radiation (c) 20 cycles (d) 5 cycles.

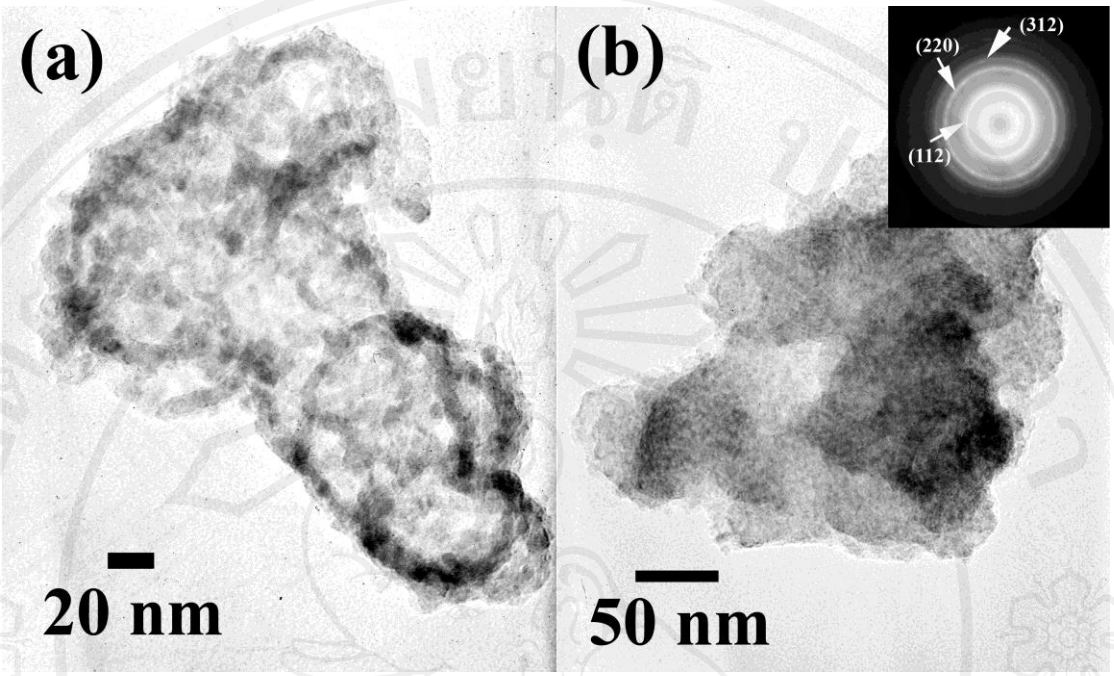

Fig. 3.28 TEM images and SAED patterns of sample CA-2 synthesized at 40 cycles of cyclic microwave radiation.

Table 3.13 Ring diffraction pattern values of $CuFsS_2$ produced under microwave radiation 40 cycles, microwave power 300 W, CA-1 sample

Ring No.	**Diameter (mm)**	**Radius (R) (mm)**	**d = L*λ/R (Å) (calculated)**	**d (Å) (JCPDS file No. 43-1479)**	**(hkl)**
1	16.4	8.20	3.0442	3.0362	112
2	19.2	9.60	2.6003	2.6060	004
3	26.5	13.25	1.8840	1.8700	220
4	31.0	15.50	1.6105	1.5926	312
5	33.2	16.60	1.5038	1.5193	224

Table 3.14 Ring diffraction pattern values of $CuFsS_2$ produced under microwave radiation 40 cycles, microwave power 300 W, CA-2 sample

Ring No.	Diameter (mm)	Radius (R) (mm)	d = L*λ/R (Å) (calculated)	d (Å) (JCPDS file No. 43-1479)	(hkl)
1	16.4	8.20	3.0442	3.0362	112
2	26.5	13.25	1.8840	1.8690	220
3	31.0	15.50	1.6105	1.5916	312

Raman spectrums of $CuFeS_2$ samples are shown in Figure 3.29, four Raman shifts produced from CA-1 and CA-2 samples are in accordance with the previous report [90]. A slight difference of Raman peaks is observed by a systematic downshift of Raman peaks of sample CA-1 by comparison with sample CA-2. For Raman spectra of crystals, the band positions and relative band intensity may vary slightly from one spectrum to another due to the orientation of the crystal lattice (and optical properties of the crystal) and/or the presence of local impurities or defects in the crystal structure [90-91].

The XPS spectrum of sample CA-1 and CA-2 are shown in Figure 3.30. The peaks can be assigned to copper, iron or sulfur. The Cu2p core-level spectrum (Figure 3.30a) show the analyzed value of binding energy of $Cu2p_{3/2}$ (932.3-932.5 eV) and the binding energy of $Cu2p_{1/2}$ (952.2-952.5 eV) peaks are close to the reported values for Cu^{+} [92]. There is no $Cu2p_{3/2}$ satellite peak around 942 eV which is attributed to Cu^{2+} was detected [93]. For the Fe2p core-level spectrum (Fig. 3.30b), the binding energy of $Fe2p_{3/2}$ (711.3-711.5 eV) and $Fe2p_{1/2}$ (725.8-726.2 eV) are in good

agreement with the reported values for Fe^{3+} [94]. The S2p core-level spectrum (Fig. 5c) reveals the binding energy of $S2p_{3/2}$ (162.5-163.3 eV), which is consistent with the reported value by several research [93-94]. However, there is a peak around 169.0-169.1 eV which might comes from the oxidized part of sample because of sample preparation in the air. The minor peaks including carbon (C1s, 284.5-285.3 eV) and oxygen (O1s, 531.3-531.5 eV) were also obtained due to the coated C for improvement of the conductivity for XPS analysis and absorbed gaseous molecules. Therefore, the valence states for synthesized $CuFeS_2$ by the XPS analysis is might be Cu^{+}, Fe^{3+} and S^{2-}.

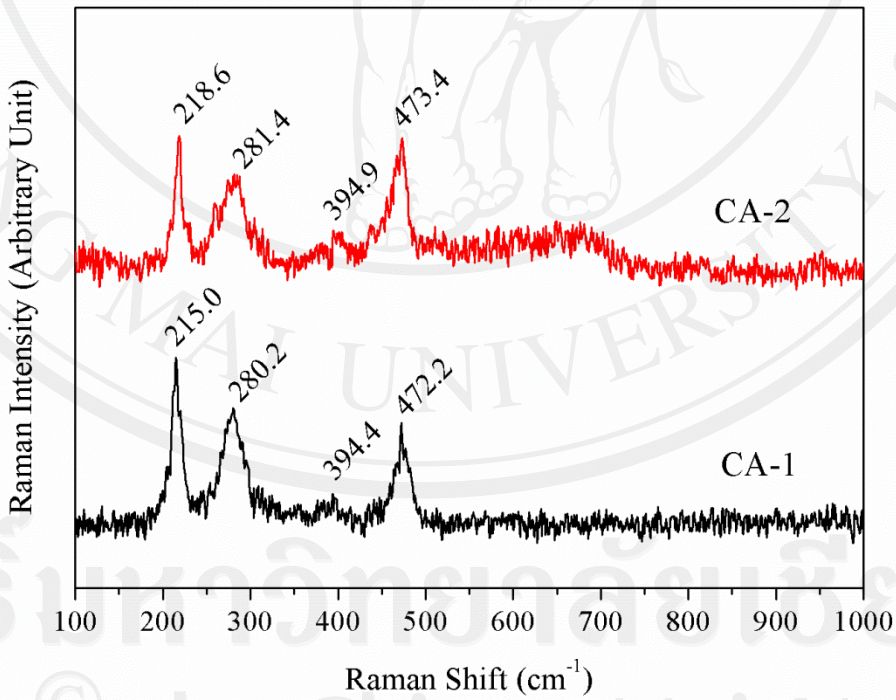

Figure 3.29 Raman spectra of $CuFeS_2$ sample CA-1 and sample CA-2 produced at 300 W CMR, 40 cycles.

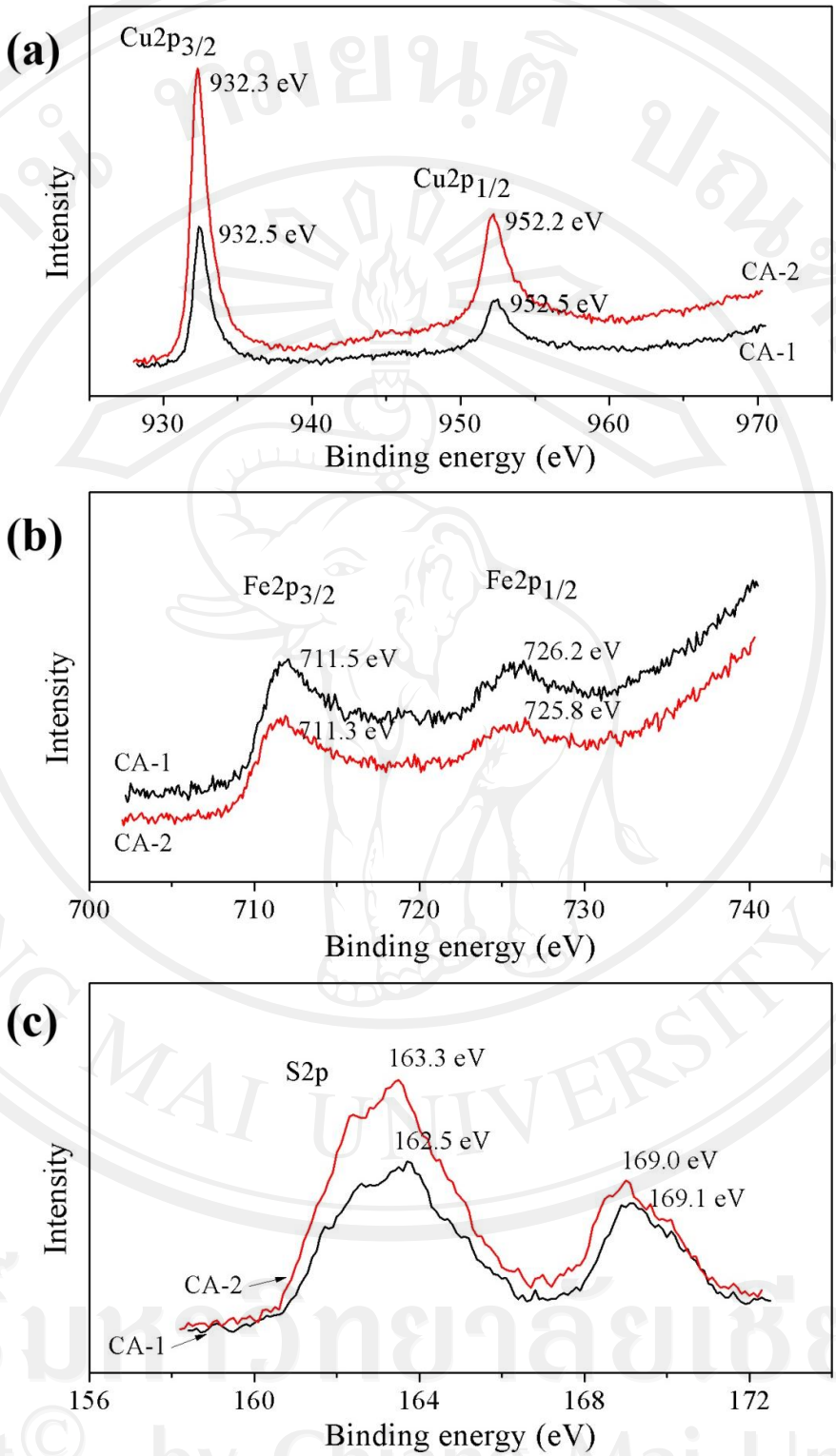

Figure 3.30 XPS measurement of $CuFeS_2$ sample CA-1 and sample CA-2 synthesized at 300 W CMR, 40 cycles.

For synthesis of $CuFeS_2$, Cu-source, Fe-source and L-cysteine were mixed in ethylene glycol. As a result of XPS, $CuFeS_2$ has the valence states Cu^+, Fe^{3+} and S^{2-}. Thus complexes of precursor were possibly formed.

$$Cu^{+} + \text{L−cysteine} \xrightarrow{coordination} [\text{Cu(L−cysteine)complexes}]$$

$$Fe^{3+} + \text{L−cysteine} \xrightarrow{coordination} [\text{Fe(L−cysteine)complexes}]$$

Alternately, [Cu–Fe(L-cysteine) complexes] could possibly form by the reaction

$$(Cu^{+}) + (Fe^{3+}) + \text{L−cysteine} \xrightarrow{coordination} [\text{Cu−Fe(L−cysteine)complexes}]$$

During the microwave radiation process, these complexes were then decomposed and $CuFeS_2$ nuclei were produced.

$$[\text{Cu(L−cysteine)complexes}] + [\text{Fe(L−cysteine)complexes}] \xrightarrow{decomposition} CuFeS_2(\text{nuclei})$$

After that, these nuclei grew to form $CuFeS_2$ nanoparticles. Then the agglomeration of $CuFeS_2$ nanoparticles occurred to reduce the surface energy of nanoparticles and follow with the growth of hollow structure in $CuFeS_2$. In this research, Cu-source and Fe-source play an important role in the phase and morphology formation of $CuFeS_2$ nanoparticles. Hollow structure was completely produced by Fe^{3+} while Fe^{2+} gives the lower crystalline $CuFeS_2$ nanoparticles with initial state of hollow structure.

In sample CA-1 and CA-2, the $Cu(CH_3COO)_2$ was employed and probably reduced by the solvent. Ethylene glycol is well known as reducing agent which could reduce metal ion to be metal[97-98]. Cu^{2+} might have been reduced to Cu^{+} intermediate ion [99-100] following with rapid reaction of Cu^{+} with L-cysteine to form a complex of precursor.

$$Cu^{2+} + e^{-} \xrightarrow{+EG} Cu^{+}$$

Fe^{3+} also could have been reduced to be Fe^{2+} by ethylene glycol, however in this research, the excess amount of Fe^{3+} was add into the mix solution. Hence, Fe^{3+} might formed the iron complex with L-cysteine quickly than Fe^{2+} which then were removed from the final solution after synthesis by washing with de-ionized water.

The Fe^{2+} from $FeCl_2.4H_2O$ was oxidized to be Fe^{3+} in final product in sample CA-2, leading to doubtfulness in oxidation–reduction of Fe^{2+} and Cu^{2+} preceded in ethylene glycol solvent.